IEEE Access
Multidisciplinary | Rapid Review | Open Access Journal

Received 7 April 2026, accepted 18 April 2026, date of publication 22 April 2026, date of current version 27 April 2026.

Digital Object Identifier 10.1109/ACCESS.2026.3686360

RESEARCH ARTICLE

A Control Architecture for Energy Management and Battery Integration in a Stand-Alone Heaving Wave Energy Converter

ABDIN YOUSIF ELAMIN[1], TUANKU BADZLIN HASHFI[2], (Graduate Student Member, IEEE), OMSALAMA M. MOHAMED[3], ADDY WAHYUDIE[1,3], ADHA IMAM CAHYADI[4], MOHAMED ABDI JAMA[5], (Member, IEEE), MOHAMMAD SHAKEEL LAGHARI[3], RUHUL AMIN KHALIL[6], SAAD MEKHILEF[7], (Fellow, IEEE), AND AHMED ABDRABOU[3]

[1]National Water and Energy Center, United Arab Emirates University (UAEU), Al Ain, United Arab Emirates
[2]Department of Electrical Sustainable Energy, Delft University of Technology, 2628 CD Delft, The Netherlands
[3]Department of Electrical and Communication Engineering, United Arab Emirates University (UAEU), Al Ain, United Arab Emirates
[4]Department of Electrical Engineering and Information Technology, Engineering Faculty, Universitas Gadjah Mada, Yogyakarta 55281, Indonesia
[5]Electrical, Computer, and Biomedical Engineering (ECBE) Department, Abu Dhabi University, Abu Dhabi, United Arab Emirates
[6]Engineering Requirement Unit, United Arab Emirates University (UAEU), Al Ain, United Arab Emirates
[7]School of Science, Computing and Engineering Technologies, Swinburne University of Technology, Melbourne, VIC 3122, Australia

Corresponding author: Addy Wahyudie (addy.w@uaeu.ac.ae)

This work was supported in part by United Arab Emirates University (UAEU), United Arab Emirates, through the 2025 UAEU Center-based Grant 12R288.

ABSTRACT This paper presents an integrated control framework for a stand-alone wave energy converter (WEC) system equipped with battery storage and load-side regulation. The core of the proposed system is a supervisory energy management system (EMS) that adaptively governs the operation by transitioning between reactive control, damping control, and power-shedding modes in response to wave conditions and the battery's state of charge (SoC). To ensure efficient energy harvesting, a variable step-size maximum power point tracking (MPPT) algorithm is employed to dynamically tune the damping and stiffness coefficients of the power take-off (PTO) mechanism. The EMS operates alongside a battery-side controller responsible for regulating the DC bus voltage through controlled charging and discharging, thereby ensuring voltage stability under fluctuating sea states and load variations. A load-side controller guarantees balanced three-phase AC power delivery, maintaining sinusoidal voltage and current profiles during dynamic load conditions. The proposed control system is validated through detailed MATLAB/Simulink simulations and hardware-in-the-loop (HIL) experiments. The findings demonstrates the EMS's ability to manage power flow efficiently and maintaining safe SoC levels under high-energy conditions, while performing load disconnection during low-energy periods to prevent battery depletion. Both simulation and experimental outcomes demonstrate reliable voltage regulation, coordinated control mode switching, and effective system response to variable sea states and load demands.

INDEX TERMS Battery storage, energy management, maximum power point tracking, ocean energy, stand-alone applications, heaving wave energy.

I. INTRODUCTION

Electricity is essential for socioeconomic advancement, as stable energy systems enhance productivity and Gross Domestic Product (GDP) growth [1]. However, around 13% of the global population remains without access to electricity [2], reflecting ongoing challenges in providing affordable and reliable energy. Key barriers include limited financing for grid expansion, low population density, and sociocultural constraints [3]. Remote areas without access to power grids often rely on fossil fuels—coal, oil, and natural gas—characterized by price volatility, transport difficulties, high

The associate editor coordinating the review of this manuscript and approving it for publication was Xiaosong Hu.

operational costs, and environmental impacts [4]. Renewable energy sources (RESs) present a sustainable alternative for meeting energy needs in off-grid remote areas. Solar photovoltaics (PV) and wind turbines (WT) are among the most established renewable technologies, valued for their sustainability and site-specific adaptability. In standalone systems, maintaining a stable power supply is challenging, as PV and WT outputs often fail to meet demand due to resource intermittency and limited temporal availability [3].

In off-grid islands and coastal regions, wave energy presents a viable standalone power solution with notable benefits. They theoretically offer greater potential than many renewables due to its high-power density of 2–3 kW/m^2 and low variability when compared to wind. Additionally, their predictability and high availability, occurring approximately 90% of the time, make them well-suited to meet nighttime electricity demand [5]. Wave energy integration in off-grid regions has been studied, revealing both its promise and challenges when coupled with other RES to meet energy demand [6], [7], [8]. These Hybrid designs can improve reliability via resource complementarity, yet it adds control and operational complexity [9]. Unfortunately, there is a notable gap in research examining standalone power systems that rely exclusively on wave energy. Exploring such systems could streamline design by avoiding hybrid RES combinations for lowering costs and complexity, while enabling focused technological innovation to advance the field.

Wave Energy Converters (WECs) maximize wave energy absorption when their resonant frequency aligns with incoming wave frequencies [10]. Popular Control strategies for maximizing absorption include damping control, referred to as resistive loading, and reactive control, often termed as approximate complex-conjugate (ACC). These approaches regulate the mechanical impedance of the power take-off (PTO) system by adjusting its damping and stiffness coefficients to match the WEC intrinsic impedance, ensuring the system's velocity aligns with wave excitation forces [11], [12], [15]. Damping control involves modifying only the damping coefficient and offers benefits such as a lower peak-to-average power ratio, reduced mechanical stress, and limited stroke displacements to prevent damage in extreme conditions [13], [14]. Although simple to implement, it is less efficient than reactive control, which adjusts both PTO coefficients to enable bidirectional power flow through alternating generator and motor operation within each wave cycle. Unfortunately, this process may introduce energy dissipation losses and impose significant design and performance constraints [16], [17]. A major limitation of both methods is their dependence on wave frequency, which is challenging to determine in real-time due to constantly changing wave conditions.

Researchers have explored model-free controls that adjust coefficients without direct wave frequency measurements. An example is Maximum Power Point Tracking (MPPT), first applied to wave energy systems in 2009 [18]. Among MPPT methods, fixed-step Perturbation and Observation (P&O) is the most frequently utilized and serves as a benchmark for other algorithms [19]. MPPT-based damping control has been investigated in several studies, such as in [20] and [21], where MPPT determined the duty cycle of boost converters for optimal energy extraction. A study [22] examined key factors affecting MPPT-based damping control in wave energy applications. The works of [23] applied a hill-climbing MPPT for reactive control by tuning damping and stiffness to maximize energy capture, while [24] introduced a variable step-size MPPT to optimize these parameters for peak WEC output. Adaptive and nonlinear MPPT approaches, commonly used in reactive control, improve tracking accuracy and enhance robustness to disturbances. However, they often require accurate system models and involve higher computational effort [25]. Optimization-based MPPT methods such as genetic algorithms have been applied in both damping and reactive control schemes to improve energy extraction under system constraints. These methods increase complexity and often rely on wave estimation techniques [26]. In addition, recent reviews show that hybrid MPPT strategies can achieve higher efficiency and robustness than conventional methods, but their practical use is limited by implementation complexity and reduced suitability for real-time operation [27]. Despite these advancements, no existing study has investigated an MPPT framework capable of seamlessly transitioning between reactive and damping control modes.

Relying solely on standalone Wave Energy Converters (WECs) is not practical because wave energy depends on sea conditions rather than consumer demand, leading to intermittency, unpredictability, and non-dispatchability [29]. Additionally, it experiences greater short-term fluctuations compared to wind energy, with its power output averaging zero twice per wave cycle [30]. Hence, an electric energy storage (EES) is needed to mitigate wave energy fluctuations, ensure a stable and continuous power supply, meet load demand, and enhance transient stability. Different types of ESSs were introduced such as hydraulic storage [31], supercapacitors [32], batteries [33] and hybrid systems [34]. Furthermore, control and power challenges posed by WEC intermittency and ESS dynamics requires an energy Management System (EMS) at the tertiary control layer to optimize operation and supervise lower-level controls [35]. It's responsible for ensuring continuous power supply to meet load demand and protecting the ESS from operating at conditions that degrades its life span [36]. Degradation in lithium-ion batteries is governed by two main mechanisms: calendar aging and cycle aging. Calendar aging depends primarily on storage conditions such as high average SoC and temperature, whereas cycle aging is driven by Ampere-hour (Ah) throughput, depth of discharge (DOD), mean state of charge (SoC) and charge/discharge rate. Ah-throughput represents the total charge exchanged over a cell's lifetime

and is a key indicator of cycle-related degradation, but studies have shown that degradation per Ah depends strongly on the SoC window and temperature. Holistic aging models indicate that degradation per Ah increases at high SoC and large DOD [37]. Experimental studies on Li(NiMnCo)O_2/graphite cells confirm that high SoC storage accelerates capacity fade and that deeper cycling intensifies degradation [39]. Cycle-life analyses further show that capacity loss follows a power-law dependence on Ah-throughput and temperature consistent with SEI-driven lithium consumption [40]. Degradation diagnostics demonstrate that both internal resistance growth and capacity fade are strongly affected by SoC range and cycling conditions [38]. In practical power-system applications battery lifetime depends on DOD and operating temperature and complete discharge reduces service life [41]. In this work, SoC is chosen as the primary supervisory variable for EMS owing to its ease of measurement and controllability. Limiting the SoC window helps constrain high DoD, voltage stress, and aggressive cycling. As reported in [42], a 20–80% SoC range can help mitigate high-voltage stress and deep discharge while preserving operational flexibility.

Energy management systems for standalone renewable systems with battery storage have been widely studied to ensure stable power balance and DC-link regulation while preserving battery lifetime under variable operating conditions. In the works of [43], an improved EMS was implemented for a standalone PV–PEMFC–battery microgrid, where supervisory control coordinates photovoltaic generation, fuel cell contribution, and battery operation to minimize hydrogen consumption while maintaining the battery SoC within predefined limits. A centralized EMS was implemented for a standalone renewable hybrid PV and fuel cell system, where source dispatch is regulated according to SoC and load demand [44]. A PV derating strategy was adopted to prevent battery overcharging and deep discharge. In addition, a control strategy for a standalone PV–battery system operating at SoC boundaries was proposed, incorporating transition mechanisms and DC-link ripple mitigation to maintain stable supply when the battery reaches its upper or lower SoC limits [45]. Its worth noting that power variability in PV and fuel-cell systems is comparatively smoother and predictable, allowing curtailment through deviation from the maximum power point. In contrast, WECs experience stochastic hydrodynamic excitation with rapid fluctuations and high power spikes that require more robust EMS coordination.

One of the few standalone WEC studies was examined by [46], where a hybrid battery–supercapacitor system was used to smooth the oscillatory output of a paddle-type WEC and maintain a constant DC bus voltage. SoC control was achieved through frequency-based electrical power sharing. The study considered regular sinusoidal wave excitation and a single-phase DC resistive load without addressing three-phase AC loads or irregular sea states. Most EMSs for wave energy primarily focus on grid integration and output power smoothing. An EMS based on simultaneous perturbation stochastic approximation was developed for hybrid ESS integration to reduce power ramp rates at the point of common coupling and improve battery lifetime through optimized power allocation [47]. Furthermore, a hierarchical wave-to-grid control scheme combining finite control set model predictive control with a supervisory EMS was introduced to maintain battery SoC within defined limits [48]. In these studies, the WEC operates at maximum energy extraction while battery SoC is regulated by adjusting the power delivered to the grid. The grid ensures frequency and PCC voltage stability and provides inertial support with the ability to absorb or supply power imbalance. Thus, WEC generation does not require strict load matching, whereas standalone systems must internally regulate power balance, voltage stability, and storage protection [9].

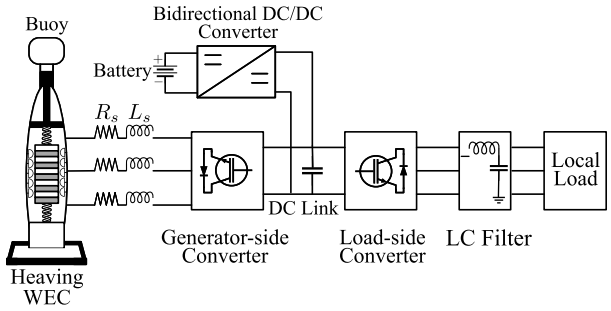

FIGURE 1. The overall system schematic.

The main contribution of this study is to design a control framework that optimizes power flow management and battery integration for standalone WEC systems in remote coastal areas. An EMS is responsible for adjusting wave energy extraction by switching between reactive and damping control based on battery SOC to prevent overcharging, deep discharging or excess power wastage. The reactive and damping controls are implemented using a variable step-size MPPT algorithm proposed in [24]. The load-side controller ensures stable voltage and frequency levels to ensure reliable power supply to local loads under varying wave conditions. Finally, a battery storage controller regulates the charge-discharge process to balance power fluctuations between WEC generation and load demand while ensuring the stability of the DC bus voltage. The paper is structured as follows: Section II describes the WEC system and its subsystems; Section III details the proposed EMS and control strategies; Section IV presents simulation results; Section V provides experimental validation; and Section VI concludes the work.

II. SYSTEM DESCRIPTION

This section presents the mathematical model of the WEC system shown in Fig. 1. The floating buoy converts vertical wave motion into linear motion that drives the Permanent

Magnet Linear Generator (PMLG) to generate electricity. The PMLG output terminals are connected to an AC load through a back to back converter topology. This topology contains two distinct converters with a DC link serving as the intermediary interface. The first converter is an AC/DC converter and is referred to as the generator-side converter, while the other is a DC/AC converter, known as the load-side converter due to its direct connection to the load. Finally, a battery storage is connected at the DC bus via a DC/DC power converter to balance between generated power and load demanded power. For model simplification, the system is divided into three subsystems; i) generator-side subsystem, ii) load-side subsystem, iii) battery storage subsystem, each described in the following subsections.

A. GENERATOR-SIDE SUBSYSTEM MODEL

This model describes wave-buoy hydrodynamic interactions and their impacts on the electrical characteristics of the power take-off (PTO) mechanism. The PTO mechanism is the device that converts the buoys' mechanical motion into electrical power, and is classified as hydraulic, pneumatic, direct-mechanical drive, or direct-electrical drive types [49]. Hydraulic PTOs employ cylinders to pressurize fluid that drives a hydraulic generator, while pneumatic systems use compressed air. Direct-mechanical drive systems convert the oscillatory motion of a buoy into rotary motion using mechanical assemblies, such as gearboxes or slider-crank linkages, that drive a rotating electrical generator. When gearboxes are employed, mechanical friction introduces losses, reducing efficiency to about 0.6–0.8, with 20%–40% of input energy dissipated as heat [50]. Nevertheless, they can achieve relatively high efficiencies of up to 81.2% in bench tests [51] and 62.4% when integrated with a WEC prototype [52]. Direct-electrical drives employ permanent magnet linear generators (PMLGs) to eliminate intermediate conversion complexities and cost. While previous studies have optimized PMLGs to reach efficiencies as high as 96% under ideal conditions [53], the work of [54] accounted for non-ideal conditions and reported PMLG efficiencies between 79% and 88%, depending on the control strategy. Furthermore, the reactive MPPT control in [24] achieved conversion efficiencies between 80% and 54%, decreasing with higher wave power levels. This aligns with [51], which attributes reduced PMLG efficiency at larger power scales to air-gap tolerance and translator stroke limitations. It is worth noting that reported PTO efficiencies vary significantly, as they are strongly influenced by device design, size, operating conditions, and control methodology, thereby making the efficiencies of different PTO mechanisms not directly comparable. In this study, the PMLG is preferred for remote standalone applications due to its reliability, simplified control architecture, lower mechanical failures, and reduced maintenance requirements [49]. Figure 2 shows the structure of the PMLG, whereas Fig. 3 illustrates the generator-side subsystem.

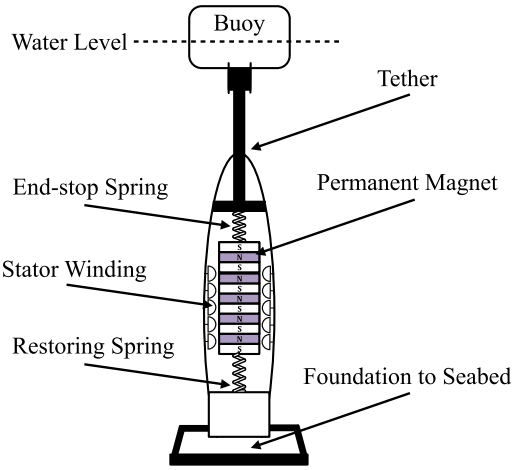

FIGURE 2. The structure of the permanent magnet linear generator and heaving buoy.

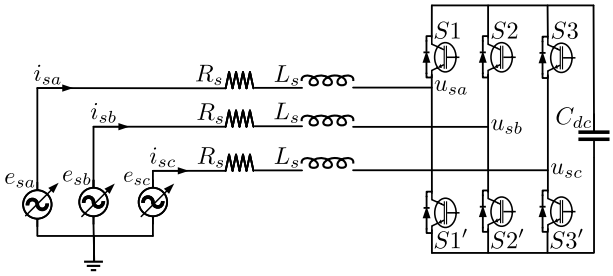

FIGURE 3. Generator-side schematic.

Assuming only vertical buoy motion, its dynamics are described using Newton's law of motion as follows

$$(M + \mu(\omega))\, a(t) + \beta_{rad}(\omega) v(t) - k_w z(t) - F_{es}(t) = F_{exc}(t) + F_{pto}(t) \quad (1)$$

where M, $z(t)$, $v(t)$, and $a(t)$ denote the buoy mass, displacement, velocity, and acceleration, respectively. The excitation force F_{exc} arises from wave-induced pressure on the buoy surface, while the control force $F_{pto}(t)$ is applied by the PTO to govern WEC motion. $\mu(\omega)$ and $\beta_{rad}(\omega)$ represent the added mass and radiation damping (resistance) coefficients, respectively, and are dependent on wave frequency ω. The former addresses inertial force caused by water mass and the latter results in a radiation force that describes energy loss due to radiated waves which is linearly proportional to velocity. The stiffness term k_w combines hydrostatic buoyancy and restoring spring forces that return the buoy to equilibrium ($z = 0$) after displacement, expressed as

$$k_w = A\rho g + K_t \quad (2)$$

where A, ρ, g, and K_t represent the buoy area, sea water density, gravitational acceleration, and restoring spring stiffness, respectively. $F_{es}(t)$ denotes the end-stop spring force that prevents the PMLG translator from impacting the enclosure at maximum stroke and is modeled as a dead-zone

nonlinear force, as expressed in [12]

$$F_{es}(t) = K_{es}\left(z(t) + \mathrm{sgn}(z(t))\, z_l\right) h\left(|z(t)| - z_l\right) \tag{3}$$

where K_{es}, z_l, sgn and h denote the end-stop spring stiffness coefficient, the maximum permissible stroke displacement, the sigmoid function and the Heaviside function, respectively. The $f_{es}(t)$ limits excessive translator motion and smooths deceleration near stroke limits during high-energy absorption, thereby preventing mechanical impacts and mitigating current and voltage spikes. By neglecting the nonlinear force term and applying Fourier transform, (1) can be expressed in the frequency domain as follows

$$\Upsilon(\omega)V(\omega) = F_{exc}(\omega) + F_{pto}(\omega) \tag{4}$$

where

$$\Upsilon(\omega) = \left(\omega(M + \mu(\omega)) + \beta_{rad}(\omega) - \frac{A\rho g + K_t}{\omega}\right). \tag{5}$$

$F_{exc}(\omega)$, $F_{pto}(\omega)$, and $V(\omega)$ are the Fourier transforms of the excitation force, control force, and buoy velocity, respectively. By rearranging (4), the transfer function from the combined forces, $F_{exc}(\omega)$ and $F_{pto}(\omega)$, to $V(\omega)$ is obtained as

$$\frac{V(\omega)}{F_{exc}(\omega) + F_{pto}(\omega)} = \frac{1}{Z_i(\omega)} \tag{6}$$

where $Z_i(\omega)$ is the WEC intrinsic impedance, given by

$$Z_i(\omega) = (M + \mu(\omega))\,\omega + \beta_{rad}(\omega) - \frac{A\rho g + K_t}{\omega}. \tag{7}$$

The coupling introduced by the tether moves the PMLG rotor, called the translator, with respect to the buoy motion. Thus, the electrical angular speed $\omega_e(t)$ is proportional to $v(t)$ and is given by

$$\omega_e(t) = \frac{\pi}{\tau_p} v(t) \tag{8}$$

where τ_p is the pole pitch of the PMLG.

The alternating magnetic flux in the stator coils caused by the rotor motion is expressed as

$$\psi(t) = \psi_{pm} \sin\left(\frac{\pi}{\tau_p} z(t)\right) \tag{9}$$

where ψ_{pm} denotes the permanent magnetic flux linkage.

According to Faraday's law, this varying magnetic flux induces electromotive force (EMF) voltages in the stator coils, which are given by:

$$e_{sa}(t) = -N\psi_{pm}\omega_e(t) \sin\left(\frac{\pi}{\tau_p} z(t)\right) \tag{10}$$

$$e_{sb}(t) = -N\psi_{pm}\omega_e(t) \sin\left(\frac{\pi}{\tau_p} z(t) - \frac{2\pi}{3}\right) \tag{11}$$

$$e_{sc}(t) = -N\psi_{pm}\omega_e(t) \sin\left(\frac{\pi}{\tau_p} z(t) + \frac{2\pi}{3}\right) \tag{12}$$

where N is the number of coil turns.

The PMLG electrical model in the *abc* reference frame can be described by:

$$e_{sk}(t) = R_s i_{sk}(t) + j\omega_e(t) L_s i_{sk}(t) + u_{sk}(t) \quad \forall\, k = a, b, c \tag{13}$$

where $i_{sk}(t)$ is the three-phase stator current, R_s is the stator resistance and $u_{sk}(t)$ is the output voltage of phase k. L_s represents the per-phase stator inductance, defined as the summation of the leakage inductance L_{ls} and the mutual inductance L_m between phases. Assuming the PMLG uses a surface-mounted design that provides a uniform air-gap and minimal magnetic saliency, resulting in a nearly symmetrical magnetic circuit when operating under balanced sinusoidal excitation. Consequently, the direct- and quadrature-axis inductances are nearly identical, allowing the stator inductance to be represented by a single equivalent value ($L_s \approx L_{sq} \approx L_{sd}$) [55]. This provides an accurate and computationally efficient representation for current control and system analysis.

Using Park transformation, the three-phase voltage and current quantities are transformed to the synchronous *dq* reference frame as follows [56]:

$$u_{sd}(t) = -R_s i_{sd}(t) - L_s \frac{di_{sd}(t)}{dt} + \omega_e(t) L_s i_{sq}(t) \tag{14}$$

$$u_{sq}(t) = -R_s i_{sq}(t) - L_s \frac{di_{sq}(t)}{dt} - \omega_e(t)\left(L_s i_{sd}(t) - \psi_{pm}\right) \tag{15}$$

where $u_{s,dq}(t)$ and $i_{s,dq}(t)$ represent the d and q axis stator voltage outputs and stator currents, respectively, in the synchronous reference frame rotating at the electrical angular frequency $\omega_e(t)$.

The control force $F_{pto}(t)$, captured wave power $P_m(t)$, and electrical generated power $P_e(t)$ are calculated as follows:

$$F_{pto}(t) = \frac{3\pi\psi_{PM}}{2\tau_p} i_{sq}(t) \tag{16}$$

$$P_m(t) = F_{pto}(t)\,\dot{z}(t) = \frac{3\pi\psi_{PM}}{2\tau_p} i_{sq}(t) v(t) \tag{17}$$

$$P_e(t) = \frac{3}{2}\left(u_{sd}(t) i_{sd}(t) + u_{sq}(t) i_{sq}(t)\right). \tag{18}$$

B. BATTERY STORAGE MODEL

In this paper, the model used to describe the electrical characteristics of the battery cells is based on the first-order Thevenin model [57]. This model includes a parallel resistor–capacitor branch, R_1 and C_1, in series with an intrinsic battery resistance R_o, as shown in Fig. 4. The addition incorporates transient voltage dynamics and polarization effects during charging and discharging. The terminal output voltage can be given by

$$v_{bat}(t) = v_{ocv} - i_{bat} R_o - i_{bat} R_1 \left(1 - e^{-t/(R_1 C_1)}\right), \tag{19}$$

where $v_{bat}(t)$, $v_{ocv}(t)$, and $i_{bat}(t)$ represent the battery output voltage, open-circuit voltage, and output current, respectively.

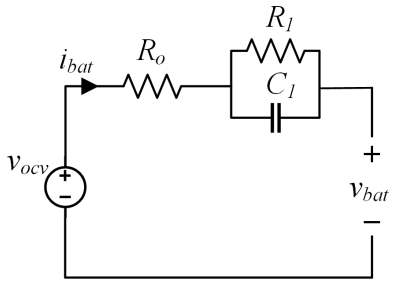

FIGURE 4. First order Thevenin battery model.

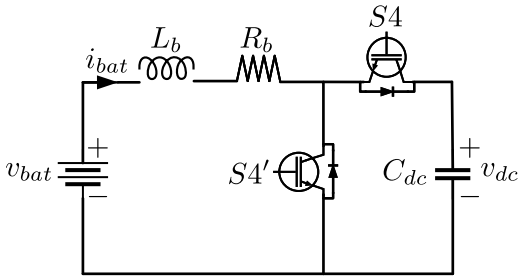

FIGURE 5. Battery storage schematic.

The state of charge (SoC) is the predominant metric used to assess a battery's energy state, where 0% signifies a completely discharged battery and 100% indicates a fully charged one. The SoC delineates the degree of charge relative to the battery's maximum capacity and is computed as

$$\mathrm{SoC}(t) = \mathrm{SoC}^{in}\left(1 - \frac{1}{Q}\int i_{bat}(t)\,dt\right) \times 100\% \tag{20}$$

where Q is battery capacity and SoC^{in} is initial state of charge. This estimation approach, referred to as the Coulomb counting–based method, is straightforward to implement; however, its accuracy is highly dependent on SoC^{in}, which may be subject to estimation errors. Alternative estimation methods include the open-circuit voltage approach, which determines SoC from the OCV–SoC relationship obtained through offline characterization but is impractical for real-time use due to the required rest period. Model-based filtering methods, such as Kalman and particle filters, utilize dynamic battery models whose accuracy depends on reliable parameter identification. Data-driven approaches, including neural networks, learn the nonlinear relationship between measurable variables and SoC without explicit physical modelling. Unfortunately, their performance relies heavily on the quality and diversity of training data. A comparative study in [58] evaluated the performance of various algorithms within the latter two categories. In this paper, the Coulomb counting method in Eq. (20) is employed, with the SoC^{in} defined as a design parameter rather than estimated. This manner mitigates errors associated with the method's sensitivity to the initial SoC and simplifies EMS testing across various initial SoC scenarios.

The model also includes a high-frequency inductor L_b and a bidirectional DC/DC converter comprising two IGBT switches, S_4 and S_4', as illustrated in Fig. 5. This energy storage operates in two modes, determined by the DC link voltage v_{dc}, namely the charge and discharge modes.

The equations that govern these operation modes are given by:

During the discharging:

$$L_b\frac{di_{bat}(t)}{dt} = -R_b i_{bat}(t) + v_{bat}(t) \tag{21}$$

$$C_{dc}\frac{dv_{dc}(t)}{dt} = i_{wec}(t) - i_l(t) \tag{22}$$

During the charging:

$$L_b\frac{di_{bat}(t)}{dt} = -R_b i_{bat}(t) - v_{dc}(t) + v_{bat}(t) \tag{23}$$

$$C_{dc}\frac{dv_{dc}(t)}{dt} = i_{wec}(t) - i_l(t) - i_{bat}(t) \tag{24}$$

where L_b and R_b denote the inductance and intrinsic resistance of the high-frequency inductor, respectively. C_{dc} represents the DC link capacitor, $i_{wec}(t)$ is the DC current generated by the WEC, and $i_l(t)$ denotes the DC current delivered to the load. Defining an appropriate v_{dc} is essential for ensuring efficient power conversion and stable WEC operations. The selected voltage must balance converter efficiency, current stress, and PMLG scalability while supporting control capabilities. Furthermore, commercially available IGBT-based converters span a wide range from 600 V up to 6500 V, handling currents from 600 A –3600 A [59]. This provides a flexible options for implementing suitable DC-link configurations in low- to high-power systems. The instantaneous power absorbed or released by the battery is given by

$$P_{bat}(t) = v_{bat}(t) \cdot i_{bat}(t). \tag{25}$$

C. LOAD-SIDE SUBSYSTEM MODEL

The load-side subsystem includes end-use loads and filters that maintain power quality and load compatibility. As shown in Fig. 6, it interfaces the DC link through a DC/AC converter, while an LC filter at the AC output mitigates high-frequency switching harmonics to improve injected power quality. The load is modeled as a balanced three-phase resistive network, typical in standalone systems for steady-state and dynamic analysis. According to Kirchhoff's voltage and current laws, the load-side subsystem model in the *abc* reference frame can be written as

$$L_f\frac{di_{lk}(t)}{dt} = u_{lk}(t) - v_{lk}(t) - R_f i_{lk}(t) \tag{26}$$

$$C_f\frac{dv_{lk}(t)}{dt} = i_{lk}(t) - i_{ok}(t) \tag{27}$$

for all $k = a, b, c$ where C_f, L_f, and R_f represent the capacitance, inductance, and equivalent series resistance of the LC filter, respectively. The variable $u_{lk}(t)$ represents the three-phase voltage at the inverter output terminals, while $v_{lk}(t)$ denotes the voltage across the capacitor terminals,

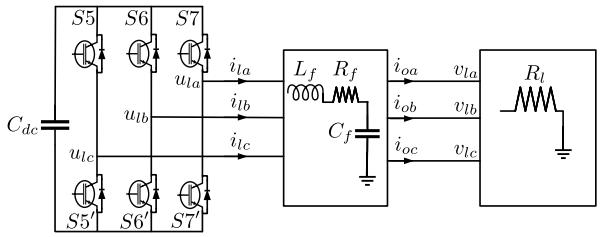

FIGURE 6. Load-side subsystem schematic.

identical to the load voltages. The current flowing through the filter inductor is represented by $i_{lk}(t)$, and $i_{ok}(t)$ denotes the current ultimately supplied to the load.

Using Park transformation, (26) and (27) can be rewritten in the dq reference frame as

$$L_f \frac{di_{ld}(t)}{dt} = u_{ld}(t) - v_{ld}(t) - R_f i_{ld}(t) + \omega_g(t) L_f i_{lq}(t) \tag{28}$$

$$C_f \frac{dv_{ld}(t)}{dt} = i_{ld}(t) - i_{od}(t) + \omega_g(t) C_f v_{lq}(t) \tag{29}$$

$$L_f \frac{di_{lq}(t)}{dt} = u_{lq}(t) - v_{lq}(t) - R_f i_{lq}(t) - \omega_g(t) L_f i_{ld}(t) \tag{30}$$

$$C_f \frac{dv_{lq}(t)}{dt} = i_{lq}(t) - i_{oq}(t) - \omega_g(t) C_f v_{ld}(t) \tag{31}$$

where (28) and (29) represent the equations governing the direct-axis components, whereas (30) and (31) correspond to the quadrature-axis components. The variables $i_{ld}(t)$, $u_{ld}(t)$, $v_{ld}(t)$, and $i_{od}(t)$ represent the d components of the inductor current, inverter output voltage, capacitor (load-side) voltage, and load current, respectively. Similarly, $i_{lq}(t)$, $u_{lq}(t)$, $v_{lq}(t)$, and $i_{oq}(t)$ correspond to the q components of the same physical quantities. The term $\omega_g(t)$ denotes the electrical angular frequency, and the cross-coupling terms in the equations arise from the transformation to the rotating dq reference frame. The electrical power delivered to the load is given by

$$P_l(t) = \frac{3}{2}\left(v_{ld}(t) i_{od}(t) + v_{lq}(t) i_{oq}(t)\right). \tag{32}$$

III. CONTROL ARCHITECTURE DESIGN

A key advantage of the back-to-back converter topology is its ability to support flexible control strategies by allowing independent regulation of each subsystem through dedicated converters. In this paper, the AC/DC converter is responsible for regulating the extraction of energy from the incident wave input, whereas the DC/AC converter governs the synchronization process and manages power delivery to the load. The DC/DC converter regulates the battery's charge and discharge processes to maintain DC bus voltage and balance the mismatch between generated and load power. This section outlines the control schemes for each subsystem converter and the energy management strategy designed to coordinate their operation according to load demand and battery SoC.

A. GENERATOR-SIDE CONTROL

The generator-side control system is structured as a hierarchical framework consisting of an outer loop and an inner loop. The outer loop determines the PTO control force $F_{pto}(t)$, which is then converted into a quadrature stator current reference. The inner loop tracks the reference to regulate stator currents, thereby realizing the computed $F_{pto}(t)$ that governs generator dynamics toward maximum wave energy absorption. Maximizing wave energy absorption requires a precise $F_{pto}(t)$ that drives the WEC's heave velocity into resonance with the incident wave excitation force [11]. In the frequency domain, the $F_{pto}(\omega)$ can be expressed in terms of its PTO impedance $Z_{pto}(\omega)$ and heaving velocity$V(\omega)$ as follows

$$F_{pto}(\omega) = Z_{pto}(\omega) V(\omega) \tag{33}$$

by substituting (33) into (4), equation (6) is transformed into

$$\frac{V(\omega)}{F_{exc}(\omega)} = \frac{1}{Z_i(\omega) + Z_{pto}(\omega)}. \tag{34}$$

This shows that resonance occurs when $Z_{pto}(\omega)$ matches the complex conjugate of $Z_i(\omega)$, mathematically expressed by

$$Z_{pto}(\omega) = Z_i^*(\omega) = B_{pto}(\omega) + K_{pto}(\omega) \tag{35}$$

such that

$$B_{pto}(\omega) = \beta_{rad}(\omega), \tag{36}$$

$$K_{pto}(\omega) = -(M + \mu(\omega))\omega + \frac{A\rho g + K_t}{\omega}. \tag{37}$$

Equation (35) is commonly referred to as the complex conjugate control equation, where B_{pto} and K_{pto} denote the PTO damping and stiffness coefficients, respectively. In practice, sea waves are polychromatic and consist of multiple sinusoidal components with distinct frequencies and amplitudes. Hence, applying the complex conjugate control is impractical due to difficulties in determining accurate damping and stiffness for each frequency component. Its implementation also suffers from stability issues and excessive heave motion from low B_{pto}, necessitating larger PMLGs [60]. Hence, practical suboptimal methods like damping and reactive control based on the peak frequency ω_p are preferred. Damping control defines the $F_{pto}(t)$ to be linearly proportional to the damping coefficient B_{pto} as shown in the following:

$$F_{pto}(t) = -B_{pto} v(t) \tag{38}$$

where

$$B_{pto} = \left|Z_i(\omega_p)\right|. \tag{39}$$

A key limitation of damping control is its dependence on a damping coefficient that does not compensate for the reactive component of Z_i, specifically $((M + \mu(\omega))\omega - \frac{A\rho g + K_t}{\omega})$. This prevents proper phase alignment between $v(t)$ and $F_{exc}(t)$. Reactive control addresses this issue by incorporating a stiffness coefficient, as detailed below

$$F_{pto}(t) = -B_{pto} v(t) - K_{pto} z(t) \tag{40}$$

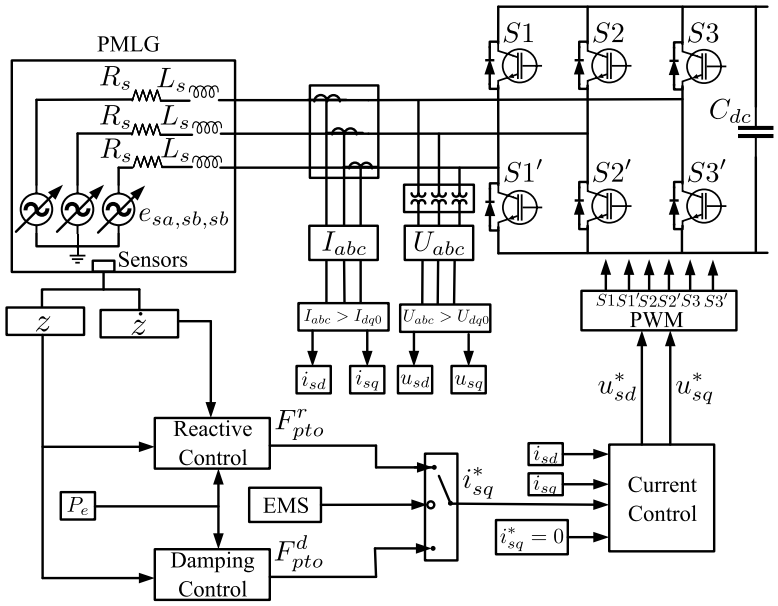

FIGURE 7. Generator-side control block diagram.

such that

$$B_{pto} = \beta_{rad}(\omega_p), \tag{41}$$

$$K_{pto} = -(M + \mu(\omega_p))\omega_p + \frac{A\rho g + K_t}{\omega_p}. \tag{42}$$

Although these suboptimal control methods can be implemented in closed-loop systems ensuring stability, accurately estimating real-time peak wave frequencies remains challenging. The study in [61] evaluates the effectiveness of the extended Kalman filter, frequency-locked loop, and Hilbert–Huang transform in estimating peak wave frequencies for tuning PTO coefficients. While these approaches improve frequency estimation accuracy, their practical implementation is hindered by computational complexity, additional sensing infrastructure, sensitivity to noise and limited consistency with spectral properties.

To overcome the need for explicit wave frequency estimation, this paper adopts the MPPT algorithm from [24] in the outer loop to realize both damping and reactive control, as illustrated in Fig. 7. The MPPT algorithm searches for the damping and stiffness coefficients in the direction of maximum power generation. The mean generated electrical power ($\bar{P}_e$) is used as the optimization target instead of the instantaneous value in (18), calculated as

$$\bar{P}_e = \frac{1}{N_s}\sum_{i=0}^{N_s} P_e(i) \tag{43}$$

where $P_e(i)$ denotes the instantaneous generated electrical power at sampling instant i and N_s is the number of samples.

The mean generated power is sampled every $T_{control}$, and coefficients are iteratively adjusted along the gradient to maximize power output. The MPPT algorithm operates under two distinct control modes:

1) **Reactive Control Mode**:
   - During odd iterations of control period k, the damping coefficient B_{pto} is updated, while the stiffness coefficient K_{pto} remains constant.
   - During even iterations, the stiffness coefficient K_{pto} is updated while B_{pto} remains unchanged.
   - The coefficient updates are defined as:

$$B_{pto}(k+1) = B_{pto}(k) + \mu(k)\cdot \text{sign}\left(\frac{\partial P_e}{\partial B_{pto}}\right) \tag{44}$$

$$K_{pto}(k+1) = K_{pto}(k) + \mu(k)\cdot \text{sign}\left(\frac{\partial P_e}{\partial K_{pto}}\right) \tag{45}$$

   with gradients approximated by:

$$\frac{\partial \bar{P}_e}{\partial B_{pto}} \approx \frac{\bar{P}_e(k) - \bar{P}_e(k-1)}{B_{pto}(k) - B_{pto}(k-1)} \tag{46}$$

$$\frac{\partial \bar{P}_e}{\partial K_{pto}} \approx \frac{\bar{P}_e(k) - \bar{P}_e(k-1)}{K_{pto}(k) - K_{pto}(k-1)}. \tag{47}$$

   - The final control force under reactive control is:

$$F^r_{pto}(t) = -B_{pto}(k)v(t) - K_{pto}(k)z(t). \tag{48}$$

2) **Damping Control Mode**:
   - B_{pto} is updated at each control period, while K_{pto} is set to zero.
   - The coefficient updates are defined as:

$$B_{pto}(k+1) = B_{pto}(k) + \mu(k)\cdot \text{sign}\left(\frac{\partial P_e}{\partial B_{pto}}\right) \tag{49}$$

$$K_{pto}(k+1) = 0. \tag{50}$$

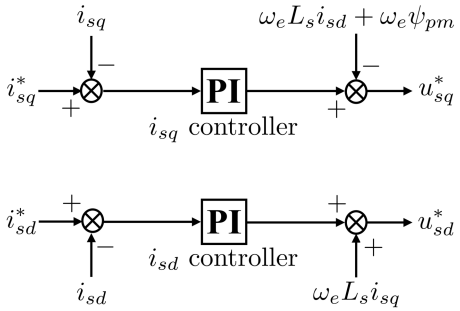

FIGURE 8. Inner current control loop structure.

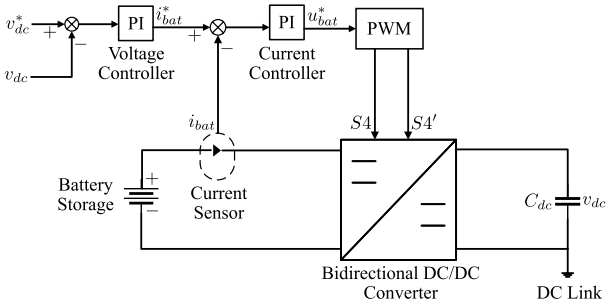

FIGURE 9. Battery control block diagram.

- The control force in damping mode simplifies to:

$$F^d_{pto}(t) = -B_{pto}(k)v(t). \tag{51}$$

The step size $\mu(k)$ determines the rate at which the MPPT algorithm responds to changes in mean generated power and is adjusted according to

$$\mu(k) = \begin{cases} \mu_{fixed}, & \text{if } \left|\Delta\bar{P}_e(k) \geq P\right| \\ \mu_{fixed} \cdot \dfrac{\left|\Delta\bar{P}_e(k)\right|}{P}, & \text{if } \left|\Delta\bar{P}_e(k) < P\right| \end{cases} \tag{52}$$

such that

$$\Delta\bar{P}_e(k) = \bar{P}_e(k) - \bar{P}_e(k-1) \tag{53}$$

where μ_{fixed} denotes the fixed step size and $\Delta\bar{P}_e(k)$ represents the change in mean generated electrical power. As mean power nears the maximum, $\Delta\bar{P}_e(k)$ drops below the power difference threshold P, reducing the step size proportionally.

The inner control loop comprises two proportional-integral (PI) controllers, each responsible for regulating one of the stator current components in the d-q reference frame, as illustrated in Fig. 8. The direct-axis current reference i^*_{sd} is assigned a value of zero to minimize copper losses, while the quadrature-axis current reference i^*_{sq} is determined by incorporating the control force calculated via the MPPT algorithm in (16). The output signals from the current controllers serve as reference values for generating the converter's output voltage components in the d-q reference frame, denoted as u^*_{sd} and u^*_{sq}, expressed as

$$\begin{aligned} u^*_{sd}(t) &= K_{dp}\left(i^*_{sd}(t) - i_{sd}(t)\right) \\ &\quad + K_{di}\int_0^t \left(i^*_{sd}(\tau) - i_{sd}(\tau)\right)d\tau \end{aligned} \tag{54}$$

$$\begin{aligned} u^*_{sq}(t) &= K_{qp}\left(i^*_{sq}(t) - i_{sq}(t)\right) \\ &\quad + K_{qi}\int_0^t \left(i^*_{sq}(\tau) - i_{sq}(\tau)\right)d\tau \end{aligned} \tag{55}$$

where K_{dp} and K_{di} denote the proportional and integral gains of the d-axis controller, respectively, while K_{qp} and K_{qi} are the proportional and integral gains of the q-axis controller. The current controllers operate at a higher sampling rate and bandwidth than the upper-level MPPT loop to ensure effective first-order hold implementation and smooth trajectories.

The PI gains are tuned using the pole-placement method described in [62], expressed as

$$K_{dp} = K_{qp} = 2\zeta\omega_n L_s - R_s, \qquad K_{di} = K_{qi} = \omega_n^2 L_s, \tag{56}$$

where ζ and ω_n denote the damping ratio and natural frequency (controller bandwidth), respectively. A higher ω_n is selected to establish appropriate bandwidth separation between the cascaded current control loops and the upper-level MPPT algorithm, thereby enabling faster current regulation and improving the system's dynamic response to sudden wave energy fluctuations. Finally, a pulse width modulation (PWM) technique is employed to convert the voltage reference signals into switching commands for the converter.

B. BATTERY STORAGE CONTROL

This control framework manages the battery charging and discharging operations to balance powers between WEC generation and load demand, storing surplus energy during highly energetic waves and supplying it under low energetic conditions. As shown in Fig. 9, it employs a cascaded architecture consisting of slower outer and faster inner control loops. The DC link voltage v_{dc} serves as a key indicator for determining the battery operating mode. The outer loop uses a proportional integral (PI) controller to regulate v_{dc}, where an increase in i_{wec} indicating excess generation raises v_{dc}, while a power deficit causes it to decrease. It compares v_{dc} with the reference v^*_{dc} and generates a battery output current reference i^*_{bat} to the inner loop. This action is governed by the proportional gain K_{po} and integral gain K_{io} as

$$\begin{aligned} i^*_{bat} = \; & K_{po}\left(v_{dc}(t)^* - v_{dc}(t)\right) \\ & + K_{io}\int_0^t \left(v_{dc}(\tau)^* - v_{dc}(\tau)\right)d\tau. \end{aligned} \tag{57}$$

The inner control loop operates at a higher sampling rate than the outer loop and continuously regulates the battery current by comparing the reference current i^*_{bat} with the measured current i_{bat}. The resulting control signal u^*_{bat} is sent to a pulse width modulation (PWM) generator, which produces switching signals for the IGBT switches in the DC/DC converter. The control signal is defined by the

proportional gain K_{pi} and integral gain K_{ii} as:

$$u^*_{bat} = K_{pi}\left(i_{bat}(t)^* - i_{bat}(t)\right) + K_{ii}\int_0^t \left(i_{bat}(\tau)^* - i_{bat}(\tau)\right) d\tau. \quad (58)$$

C. LOAD-SIDE CONTROL

In grid-connected applications, DC/AC converters primarily function as current-source inverters (CSI), managing the active and reactive power exchange. The grid inherently maintains the voltage at the point of common coupling (PCC), thereby simplifying converter control by eliminating the requirement for local voltage regulation. Conversely, during islanded operations, converters transition into a voltage-source inverter (VSI) role, taking responsibility in regulating voltage amplitude and frequency at the load terminals [63].

The latter role is assigned to the load-side control strategy to ensure a stable and uninterrupted power supply to the load. It features a cascaded configuration similar to the generator-side control. The outer loop regulates the load voltages v_{ld} and v_{lq} by generating the necessary current references i^*_{ld} and i^*_{lq} to be supplied to the load. The quadrature-axis load voltage reference v^*_{lq} is set to zero to eliminate reactive power flow under nominal load conditions. The direct-axis reference voltage v^*_{ld} is derived from the peak value of the load phase voltage, calculated from the RMS phase voltage V_{rms} as follows

$$v^*_{ld} = \sqrt{2}V_{\text{rms}}. \quad (59)$$

The PI controllers in the outer loop generate the current references i^*_{ld} and i^*_{lq} expressed below

$$i^*_{ld}(t) = K_{vp}\left(v^*_{ld}(t) - v_{ld}(t)\right) + K_{vi}\int_0^t \left(v^*_{ld}(t) - v_{ld}(t)\right) d\tau \quad (60)$$

$$i^*_{lq}(t) = K_{vp}\left(v^*_{lq}(t) - v_{lq}(t)\right) + K_{vi}\int_0^t \left(v^*_{lq}(t) - v_{lq}(t)\right) d\tau. \quad (61)$$

The inner loop determines the converter output voltage references u^*_{ld} and u^*_{lq} required to follow i^*_{ld} and i^*_{lq} as shown

$$u^*_{ld}(t) = K_{dp}\left(i^*_{ld}(t) - i_{ld}(t)\right) + K_{di}\int_0^t \left(i^*_{ld}(\tau) - i_{ld}(\tau)\right) d\tau \quad (62)$$

$$u^*_{lq}(t) = K_{qp}\left(i^*_{lq}(t) - i_{lq}(t)\right) + K_{qi}\int_0^t \left(i^*_{lq}(\tau) - i_{lq}(\tau)\right) d\tau. \quad (63)$$

where K_{dp}, K_{di}, K_{qp}, and K_{qi} denote the proportional and integral gains of the respective PI controllers. Similar to the generator-side controller, the PI controllers operate at a higher bandwidth, and their parameters are tuned using (56) by replacing the PMLG stator impedance with the filter impedance. Figure 10 depicts the block diagram of the load-side control strategy. The converter's AC outputs are synchronized at a nominal fundamental frequency of $f_0 = 50$ Hz.

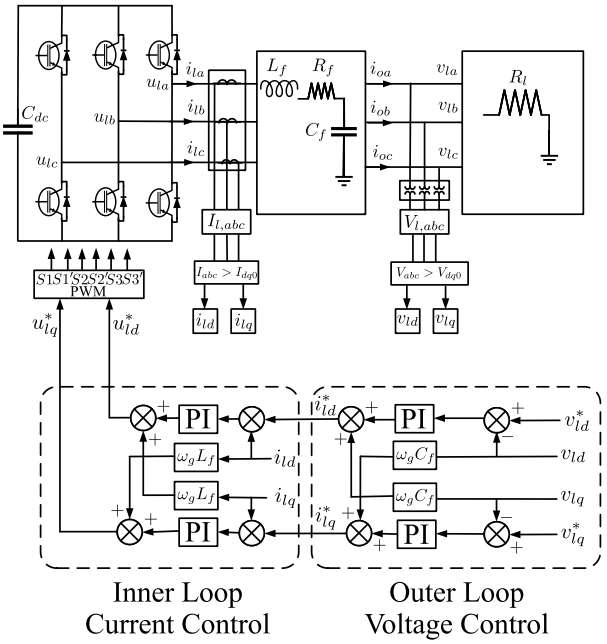

FIGURE 10. Load-side control block diagram.

The instantaneous electrical angle θ_g is obtained by applying a modulo operation to the system clock with respect to the fundamental period $T_0 = 1/f_0$. This effectively produces a repeating phase angle that progresses linearly over one 50 Hz period. This angle establishes the rotating frame for Park transforms, synchronizing the decomposition of voltage and current into d-q components at 50 Hz.

The ω_g shown in (28) - (31) can computed as

$$\omega_g(t) = \frac{d\theta_g(t)}{dt} \approx 2\pi f_0. \quad (64)$$

D. ENERGY MANAGEMENT STRATEGY

The proposed EMS manages energy flow among the WEC, battery storage, and connected loads to prevent battery overcharging and avoid power wastage [64], [65]. This EMS incorporates four distinct operational modes determined by the sea-state energy availability and battery state of charge (SoC): (1) reactive control mode, (2) damping control mode, (3) load shedding mode, and (4) WEC disconnection mode. Under typical operating conditions (SoC within defined optimal limits, $\text{SoC}_{min} < \text{SoC} < \text{SoC}_{max}$), the WEC operates at maximum power generation via reactive control, directly supplying load demands with the battery compensating for transient discrepancies. When the SOC reaches the upper limit (SoC_{max}), the EMS transitions to damping control mode, intentionally reducing WEC power generation below peak capacity to prevent battery overcharging and align production with load consumption until either the SOC reduces below SoC_{max} or load demand increases.

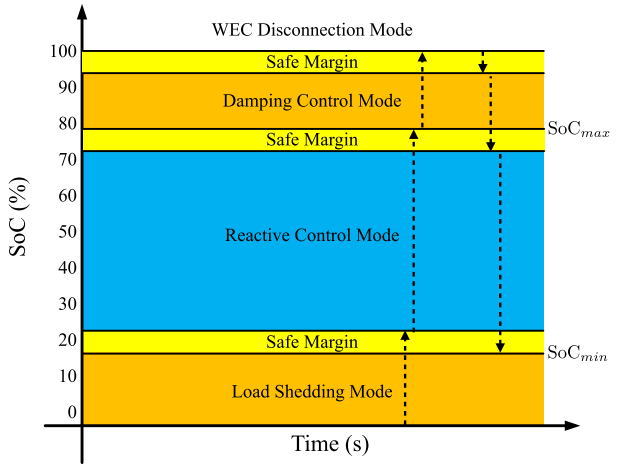

FIGURE 11. State of charge working rule.

In scenarios where the battery is fully charged (SoC = 100%) or load demand significantly decreases, the EMS initiates WEC disconnection mode, allowing the battery to discharge safely to supply the load without overcharging risks. Conversely, if the SOC drops below the lower threshold (SoC$_{min}$), the EMS enters load shedding mode, disconnecting non-critical loads to prioritize critical functions and prevent battery deep discharge, simultaneously operating the generator-side converter in reactive control mode. To improve operational stability and mitigate frequent mode switching, a safe margin (SM) is defined for transitions between state of charge (SOC) thresholds. This concept is illustrated in Fig. 11, which delineates the EMS operational modes as a function of SOC levels. The SM allows a controlled discharge or charge period before transitioning back to reactive control, particularly beneficial during prolonged periods of low energy sea states. The EMS flowchart is shown in Fig. 12.

IV. SIMULATION RESULTS

The dynamic performance of the proposed EMS and control schemes are evaluated using MATLAB/Simulink. The WEC parameters employed in the simulation model are outlined in Table 1, while Table 2 summarizes the design parameters associated with the MPPT algorithm, which facilitates both damping and reactive control operations. The MPPT is executed with a sampling interval of 40 s, whereas the PI controllers operate at a smaller interval of 1 ms to ensure precise dynamic response. The standalone system supplies two distinct electrical loads, referred to as $P_{l,1}$ and $P_{l,2}$.

These loads are connected in parallel at the point of common coupling, allowing each to operate at a common voltage level while drawing current in proportion to its individual power demand. Balanced loads are assumed, operating under standard conditions without any unbalance or transient disturbances. The evaluation begins with a comparative analysis of damping and reactive control strategies in terms of their influence on power generation.

TABLE 1. WEC system parameters.

Parameter	Symbol (value)
Total mass	M (3×10^4 kg)
Buoy diameter	D (5 m)
Buoy surface area	A (19.6 m^2)
Restoring spring stiffness coefficient	K_t (6×10^4 N/m)
End-stop spring stiffness coefficient	K_{es} (5×10^5 N/m)
Sea water density	ρ (1.025×10^3 kg/m^3)
Gravitational acceleration	g (9.8 m/s^2)
PMLG flux linkage	ψ_{PM} (19.8 Wb)
PMLG pole pitch	τ_p (4.5×10^{-2} m)
Number of turns per-phase	N (550)
PMLG stator resistance	R_s (2 Ω)
PMLG stator inductance	L_s (32 mH)
Translator stroke limit	z_s (3 m)
DC bus capacitor	C_{dc} (0.3 F)
Nominal DC bus voltage	v_{dc} (3500 V)
DC/DC Inductor resistance	R_b (30 mΩ)
DC/DC Inductor inductance	L_b (3.3 mH)
Nominal battery voltage	v_{bat} (1000 V)
Filter inductance	L_f (10 mH)
Filter capacitance	C_f (10 μF)
Nominal load rms voltage	V_{rms} (707 V)
Fundamental frequency	f_0 (50 Hz)
Nominal power of load 1	$P_{l,1}$ (20 kW)
Nominal power of load 2	$P_{l,2}$ (40 kW)

TABLE 2. MPPT control parameters.

Parameter	Symbol	Value
Control period	$T_{control}$	40 s
Fixed step-size	μ_{fixed}	2.5×10^4
Initial damping coefficient	$B_{pto}(0)$	1×10^5 Ns/m
Initial stiffness coefficient	$K_{pto}(0)$	1×10^5 N/m
Maximum damping coefficient	B_{pto}^{max}	3×10^5 Ns/m
Maximum stiffness coefficient	K_{pto}^{max}	2.5×10^5 N/m
Power difference threshold	P	5 kW

The EMS is evaluated under three irregular sea-state conditions, characterized by different combinations of significant wave height H_s and peak frequency ω_p, as shown in Table 3. These combinations are based on the works of [66], where long-term wave statistics for the Danish part of the North Sea are summarized into seven operational sea states. The three sea states are selected from this set to represent low (S1), moderate (S2), and high (S3) levels of wave power content. They are generated using the JONSWAP spectrum, which defines the spectral density $S(\omega)$ for wind-driven, fetch-limited seas [66]. The sea surface elevation $\eta(t)$ is obtained as a linear superposition of sinusoidal wave components with random phases weighted by the JONSWAP spectral density, given by

$$\eta(t) = \sum_{n=1}^{N} \sqrt{2S(\omega_n)\Delta\omega}\cos(\omega_n t + \phi_n), \tag{65}$$

where ϕ_n are uniformly distributed random phase angles, $\Delta\omega$ is the frequency increment, and ω_n denotes the angular frequency of the n^{th} wave component.

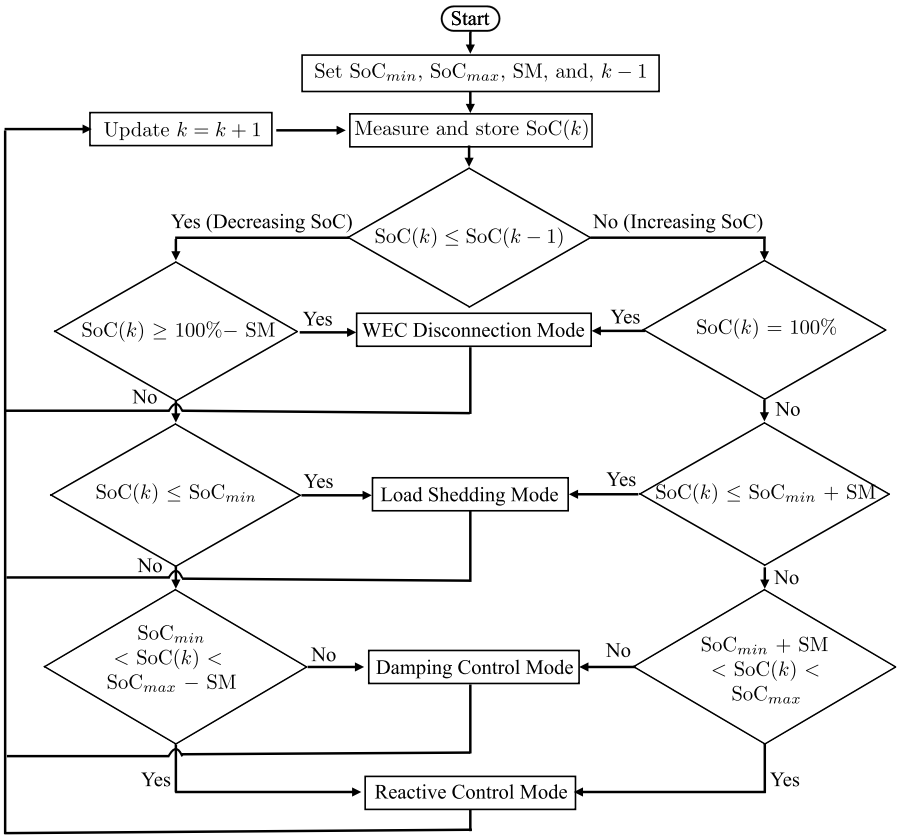

FIGURE 12. The energy management strategy flowchart.

TABLE 3. Sea state characteristics.

Parameter [unit]	S1	S2	S3
Significant height H_s [m]	1.5	3	5.7
Peak frequency ω_p [rad/s]	1	0.8	0.54

To ensure effective battery operation and longevity, the state of charge (SOC) thresholds are defined as $SoC_{max} = 80\%$ and $SoC_{min} = 20\%$, consistent with optimal SoC ranges reported in the works of [42]. In the first scenario, the SOC remains within the optimal range under a S2, resulting in the activation of the reactive control mode. The second scenario considers a S3 with the SoC nearing its upper limit, prompting the system to operate in damping control mode. In the final case, S1 is applied while the SoC approaches its minimum SoC threshold to trigger load shedding mode.

A. DAMPING CONTROL AND REACTIVE CONTROL COMPARISON

The comparative assessment is conducted under the moderately energetic sea state S2, whose characteristics are summarized in Table 3. The corresponding irregular wave elevation profile is presented in Fig. 13. Figure 14a illustrates the mean generated power, sampled at 40 s intervals in accordance with the MPPT algorithm's control period. During the initial 100 s, both control strategies produce comparable power outputs. As the MPPT algorithm iteratively adjusts the PTO coefficients, reactive control outperforms damping control, achieving a peak mean power of approximately 52.14 kW, compared to 27.93 kW under damping control. This corresponds to an average improvement of 87.44% in generated power.

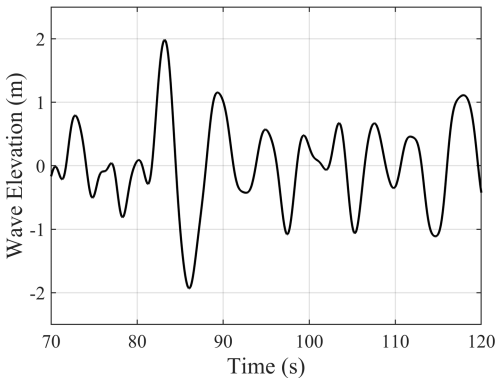

FIGURE 13. Wave elevation profile of sea state S2.

Figure 14b shows the evolution of the damping coefficient B_{pto} under both control schemes. Damping control updates only B_{pto}, increasing it from its initial value of

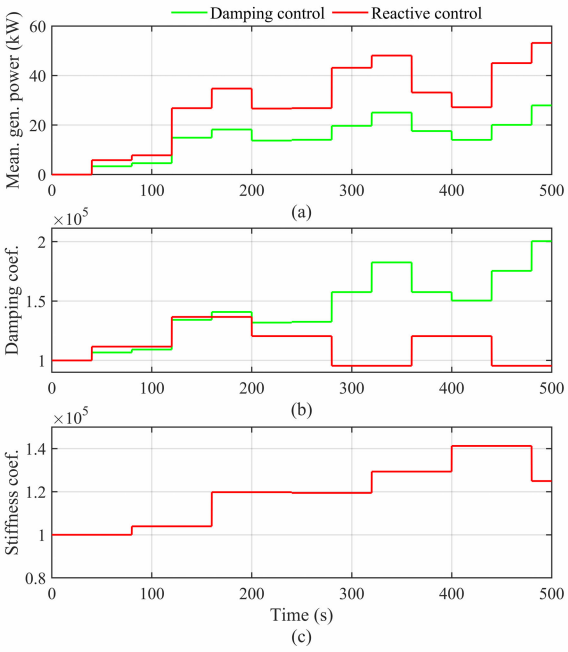

FIGURE 14. Damping versus reactive control responses under sea state S2: (a) mean generated power, (b) damping coefficient, (c) stiffness coefficient.

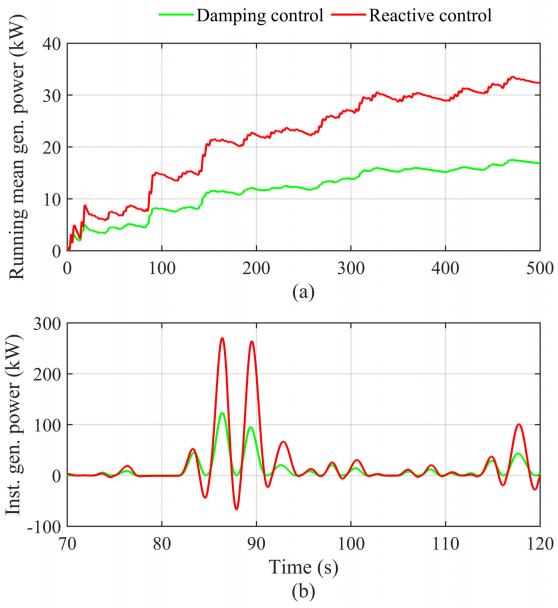

FIGURE 15. Generated power comparison during sea state S2: (a) running mean generated power, (b) instantaneous generated power.

1.0×10^5 Ns/m to approximately 2.1×10^5 Ns/m by the end of the simulation. The variation of B_{pto} closely follows the trend of mean generated power, increasing or decreasing accordingly. Smaller step sizes are observed when the power difference between successive control periods falls below the defined threshold. Furthermore, reactive control maintains a lower damping coefficient of less than 1.5×10^5 Ns/m, as it compensates energy absorption through the additional stiffness component. The K_{pto} is tuned under reactive control, as illustrated in Fig. 14c, starting from an initial value of 1.0×10^5 N/m, K_{pto} is adaptively increased to approximately 1.42×10^5 N/m.

Figure 15a presents the running mean power throughout the simulation, highlighting the superiority of reactive control, achieving 32.38 kW at the simulation's end, compared to 16.91 kW obtained with damping control. Figure 15b displays the instantaneous generated power in the interval $t = 70$–120 s. Positive values in both damping and reactive control indicate power transfer from the incident waves to the WEC; conversely, negative values occurring exclusively under reactive control signify reverse power flow resulting from reactive power exchange. Reactive control achieved a peak power of 271.2 kW at 86.4 s, surpassing damping control by 147.5 kW at the same instant. This peak coincides with a maximum wave elevation of -1.94 m, illustrating the correlation between wave elevation magnitude and generated power. Despite the occurrence of these power peaks, the PTO coefficients were not immediately updated in response to these transients. Instead, the MPPT accumulates instantaneous power samples over the $T_{control}$ interval, leading to a gradual rise in mean generated power from 7.8 kW to 26.6 kW under reactive control and from 4.5 kW to 14.9 kW under damping control, as shown in Fig. 14a. Consequently, Fig. 14b shows that the MPPT updates the damping coefficient upon completion of the averaging window, increasing it by 2.5×10^4 for both strategies at 120 s. It is recommended that T_{control} exceeds three wave periods to provide a more statistically meaningful assessment of the sea state energy level over an extended time window [23]. This reduces the influence of sudden short-term power surges and limits excessive PTO coefficient updates that could otherwise degrade MPPT stability. Nevertheless, a larger T_{control} leads to a slower MPPT response, which may delay coefficients reaching their optimal values.

Finally, a comparative analysis is conducted to assess the influence of damping and reactive control strategies on the WEC efficiency in harvesting wave energy and converting it into electrical power. The assessment is performed across all sea states listed in Table 3, using quantitative performance metrics including the mean absorbed mechanical power $\overline{P}_m$, the mean generated electrical power $\overline{P}_e$, the power take-off (PTO) efficiency η_{PTO} and the capture width ratio (CWR). The η_{PTO} defines the ratio of useful electrical power converted by the wave-induced linear motion of the PMLG, while CWR provides a dimensionless measure of the WEC's absorption ability relative to the available wave power content and buoy geometry. They are defined, respectively, as

$$\eta_{\text{PTO}} = \frac{\overline{P}_e}{\overline{P}_m} \times 100\%, \tag{66}$$

$$\text{CWR} = \frac{\overline{P}_m}{J\,D}, \tag{67}$$

where D denotes the buoy diameter and J represents the wave energy transport, defined as the wave power per unit crest

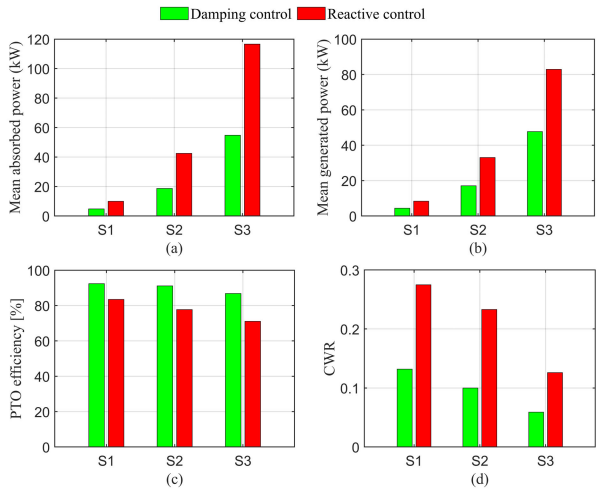

FIGURE 16. Comparative performance assessment of damping and reactive control under low, moderate, and high energetic sea states (S1–S3) in terms of: (a) mean absorbed power, (b) mean generated power, (c) PTO efficiency, (d) capture width ratio.

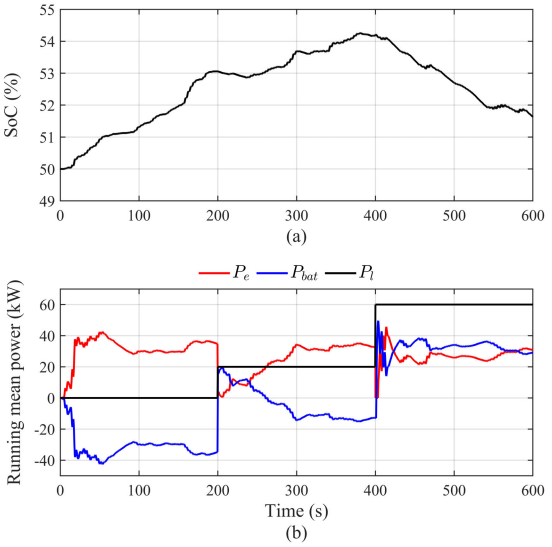

FIGURE 17. Dynamic performance of the battery under sequential load steps in S2: (a) state of charge, (b) running mean power.

width. For irregular waves, the wave energy transport can be approximated as [66]

$$J \approx 0.9 \frac{\rho g^2 H_s^2}{32\,\omega_p}, \tag{68}$$

Figure 16a presents the absorbed power under reactive control over 600 s, reaching 10.0 kW, 42.5 kW, and 116.6 kW for S1, S2, and S3, respectively. Compared with damping control, these values correspond to increases of up to 108%, 127%, and 113%. Similar gains are observed in the generated power, with reactive control exceeding damping control by approximately 91%, 94%, and 74%, as depicted in Fig. 16b. However, Fig. 16c shows that damping control consistently yields higher η_{PTO}, decreasing from 92.4% to 86.8%, whereas reactive control exhibits lower values ranging from 83.5% to 71.1% caused by its bidirectional power, during which the PMLG alternates between motor and generator operation. Furthermore, η_{PTO} reduction with increasing sea-state energy is linked to the requirement for larger control forces, which result in higher stator currents and increased copper losses. Figure 16d depicts the CWR tends to decrease with increasing wave power content, ranging from 0.275 to 0.126 under reactive control and from 0.132 to 0.059 under damping control. This behavior results from physical constraints that limit further energy absorption such as buoy size, PMLG stroke or power ratings. As these limits are approached, the gap between reactive and damping control narrows.

B. MODERATE SEA STATE CASE

Here, the WEC operates under the moderately energetic sea state S2, characterized by the parameters listed in Table 3 and the wave profile shown in Fig. 13. The simulation runs for 600 s, with the battery initially at 50% state of charge, resulting in the generator-side controller operating in reactive control mode. Figure 17a illustrates the battery's SoC in response to the running-mean trajectories of the generated electrical power P_e, battery power exchange P_{bat}, and load demand P_l in Fig. 17b. During the first 200 s, the SoC increases significantly to approximately 53% because no load is connected. Consequently, most of the power generated by the WEC is stored in the battery, as indicated by the negative values of P_{bat}. In the next 200 s, a 20 kW load is connected. Most of its demand is supplied by the WEC and the excess P_e is stored in the battery, increasing the SoC to 54.2%. After 400 s, the 40 kW load is connected and introduces a decline in SoC since P_e alone is insufficient to meet the demand and the battery must supply the deficit.

Figure 18 presents the DC bus voltage regulation and the corresponding instantaneous power flow of the standalone WEC system. In Fig. 18(a), v_{dc} remains tightly regulated around its reference value of 3500 V, exhibiting only minor oscillations despite fluctuations in the generated power, with the voltage confined between 3488 V and 3513.4 V. Figure 18(b) shows the instantaneous power profiles between 380 and 420 s, where the load demand increases from 20 kW to 60 kW at $t = 400$ s. The battery responds rapidly to compensate for the mismatch between generation and demand, maintaining the DC bus voltage near its reference. When P_e falls below the load demand, P_{bat} becomes positive to supply the deficit, whereas excess generation leads to negative P_{bat} as the battery charges. For instance, at 407.3 s, P_e decreases to -55.2 kW and the battery delivers 115.2 kW, while at 413 s, P_e reaches 197.1 kW and the battery absorbs the surplus with a charging power of -137.1 kW.

Figure 19 presents the performance of the inner current control loops of the generator-side, battery storage, and load-side controllers during a step increase in load power from 20 kW to 60 kW. In Fig. 19a, the $i_{sq}(t)$ accurately tracks its reference to realize the computed $F_{pto}(t)$ for reactive control. Figure 19 shows $i_{bat}(t)$, which exhibits a sudden rise

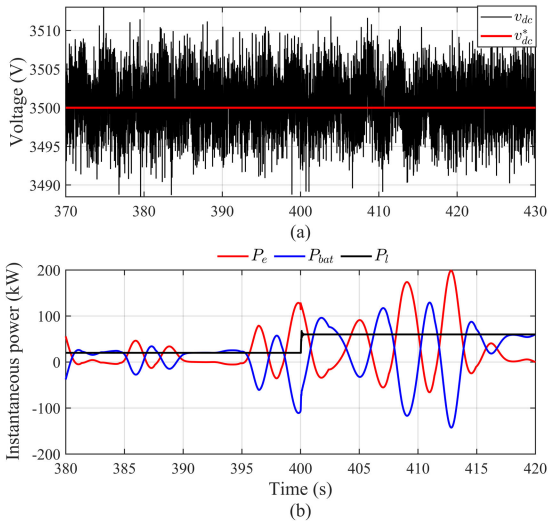

FIGURE 18. Battery Storage Controller Performance under S2: (a) DC bus voltage regulation, (b) instantaneous power flow.

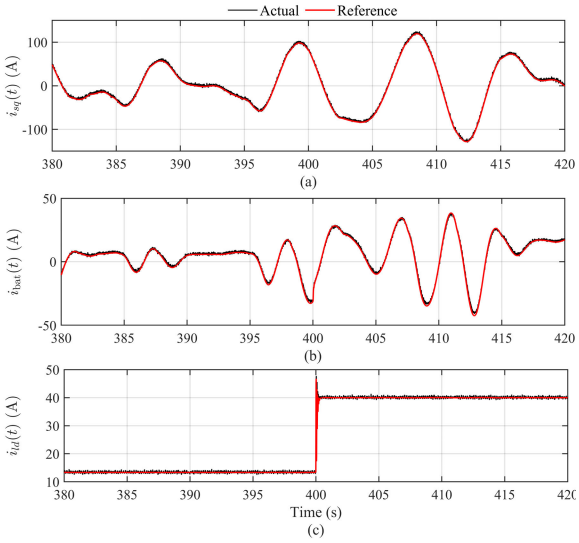

FIGURE 19. Inner current control loop performance during a load step from 20 kW to 60 kW: (a) quadrature-axis stator current tracking, (b) battery current tracking, (c) direct-axis load current tracking.

of approximately 12 A to compensate for the additional power demand at 400 s. Figure 19c depicts the direct load current $i_{ld}(t)$, which increases from 13.3 A to approximately 40 A in response to the load change. A brief overshoot reaching about 46 A is observed immediately after the transition, followed by rapid settling to the new steady-state value. The close tracking of reference and measured currents demonstrates the stability and coordinated performance of the inner current control loops during the load change.

Figure 20 shows the load-side control ability to maintain balanced three-phase operation at the PCC. Figure 20a illustrates the three-phase voltage waveforms at the PCC. The waveforms are balanced and sinusoidal, each with a peak amplitude of 1000 V, which corresponds to the nominal RMS voltage specified in Table 1. Voltages are maintained at a

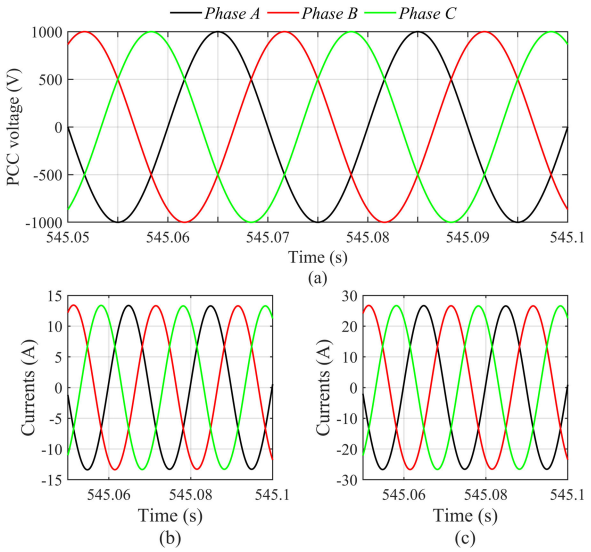

FIGURE 20. Load power quality during S2: (a) PCC voltage, (b) currents injected to load 1, (c) currents injected to load 2.

nominal frequency of 50 Hz. Figures 20b and 20c present the current waveforms for Load 1 (30 kW) and Load 2 (40 kW), respectively. The current magnitudes are higher in Load 2, consistent with the greater power requirement. Currents are synchronized with their voltages and exhibit a clean sinusoidal shape, indicating high-quality power delivery.

C. HIGH SEA STATE CASE

This case will evaluate the EMS performance under the highly energetic sea state shown in Table 3. The SoC of the battery is set at 75% and both loads are connected with a cumulative power demand of 60 kW. Figure 21a presents the SoC under the proposed EMS and compares it with pure damping and reactive control strategies. During the initial 327 s, the EMS operates in reactive control mode, resulting in a steady increase in SoC until it reaches the predefined upper threshold ($\text{SoC}_{max} = 80\%$). Upon reaching this limit, the EMS switches to damping control to reduce the generated power P_e, thereby preventing further charging. In Fig. 21, reactive control causes SoC to increase steadily and reach about 86.2% at the end of the simulation. In contrast the damping strategy leads to a continuous decrease in SoC to nearly 70%, indicating that the generated power from pure damping control does not satisfy the load demand. Figure 21b shows that the EMS transitions between reactive and damping control. The damping coefficient B_{pto} varies between 1×10^5 and 2×10^5. The stiffness coefficient K_{pto} is set to zero during damping mode. This transition keep the SoC from exceeding boundary limits by avoiding overcharging and deep discharge.

Figure 22 complements Fig. 21 by showing the running mean power profiles and clarifying how the EMS regulates power flow to maintain the SoC within its optimal range. The load demand remains constant at 60 kW throughout the simulation. The generated power P_e increases gradually

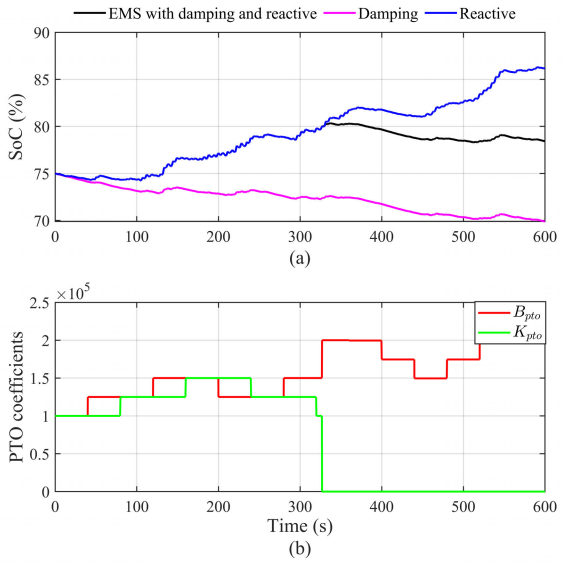

FIGURE 21. EMS performance during the transition from reactive control to damping control at S3: (a) state of charge, (b) PTO coefficients.

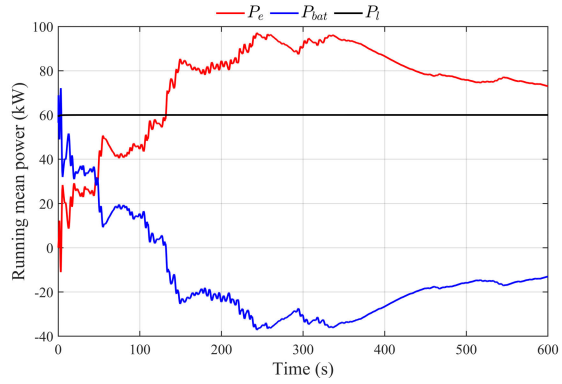

FIGURE 22. Running mean power plots during S3.

to about 95.6 kW at 334 s, then decreases as a result of the SoC reaching 80% and activating damping control. During this period P_{bat} is negative which indicates battery charging and explains the rise in SoC under reactive control. Once damping control is activated the P_{bat} approaches zero which indicates partial battery discharge to support the load.

Figure 23 provides a view of the electrical response during switching control modes under irregular wave conditions. Figure 23a shows that variations in the DC-link voltage are directly influenced by changes in the generated power represented by the generator current i_{sq}. When i_{sq} increases the generated power rises and a corresponding increase in DC voltage is observed. Although the DC bus voltage fluctuations are more pronounced than in S2 due to the higher P_e, it remains well regulated around the 3500 V reference. A closer inspection of the transition reveals a short duration transient in i_{sq}. As shown in Fig. 23b, it exhibits a drop from about −70.1 A to −213 A before rapidly settling near −98 A.

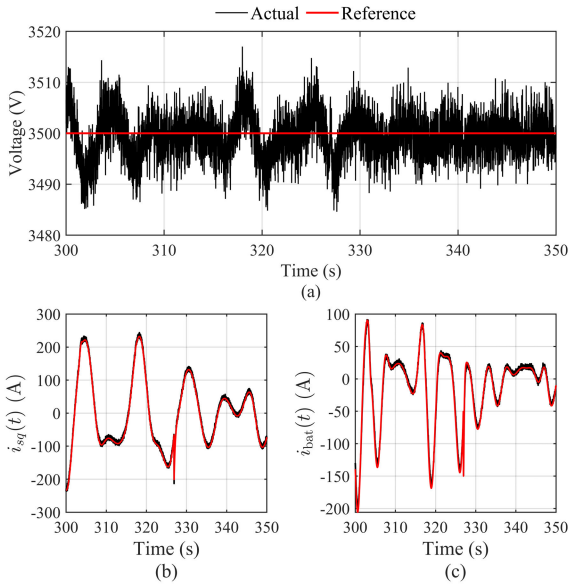

FIGURE 23. Electrical response during reactive and damping control transitions: (a) Dc bus voltage, (b) PMLG quadrature current tracking, (c) battery current tracking.

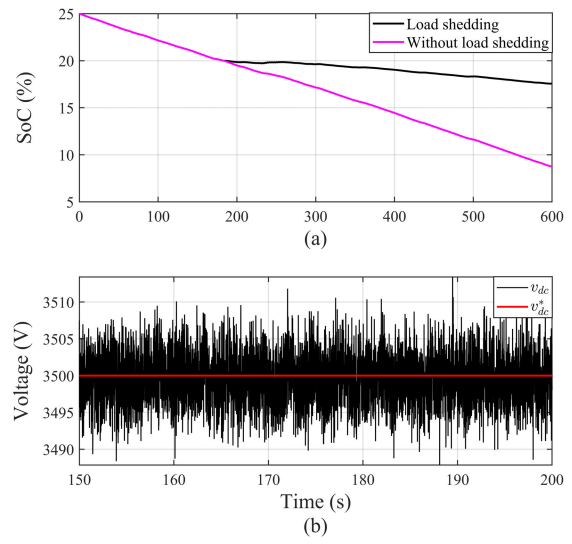

FIGURE 24. EMS performance during load shedding at S1: (a) state of charge, (b) Dc bus voltage.

This results from the sudden adjustment of the control force during switching between reactive and damping strategies. Figure 23c shows a short transient drop in i_{bat},from − 50.2 A to −149.8 A, reflecting the rapid adjustment of battery power during the switch between reactive and damping control. Due to this fast response the DC-link voltage deviates only slightly and reaches a minimum of about 3484 V before quickly returning to its nominal value. These results demonstrate that although brief current transients occur during control mode transitions they are well controlled and do not compromise DC bus voltage stability and current tracking capability.

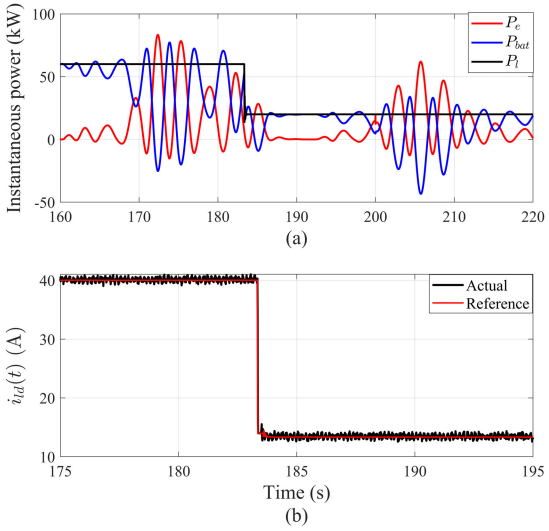

FIGURE 25. Electrical response during load shedding at S1: (a) instantaneous power plot, (b) load direct current tracking.

D. LOW SEA STATE CASE

The low-energy irregular wave S2 is considered with an initial SoC of 25% to represent limited available sea power content against the 60 kW demanded power. Figure 24a demonstrates the ability of the EMS to protect the battery through load shedding. Without load shedding, the SoC decreases continuously due to insufficient harvested wave energy and falls below 9% by the end of the simulation. Under the proposed EMS, the SoC follows a similar decline until it reaches the minimum threshold of 20% at 183.6 s. At this point, the EMS activates load shedding and disconnects the 40 kW secondary load with the 20 kW remaining, as illustrated in Fig. 25a. This strategic action significantly relieves the battery, allowing its SoC to remain above 17.7%. Figure 24b presents the DC bus voltage v_{dc} and its reference v^*_{dc} between 150 s and 200 s. The reference is set to 3500 V and the measured voltage remains regulated between 3490 V and 3510 V.

Figure 25a shows the instantaneous powers P_e, P_{bat}, and P_l during load shedding. Before load shedding at 183.6 s, P_{bat} exhibits large positive peaks to compensate for the mismatch between P_e and P_l. After the load is reduced to 20 kW, the peaks of P_{bat} decrease noticeably and negative values appear more often, indicating charging as the load demand on the battery is reduced. Figure 25b shows the i_{ld} current response. The reference current generated by the outer voltage control loop decreases from 40 A to 13.7 A, corresponding to the load reduction from 60 kW to 20 kW during load shedding. Figure 26 captures the three-phase current waveforms during a load shedding event. In Fig. 26a, the currents injected into the first load remain balanced and continuous, indicating uninterrupted supply. In contrast, Fig. 26b shows the current supplied to the second load rapidly decreasing from 183.6.4s until it reaches zero, indicating its disconnection.

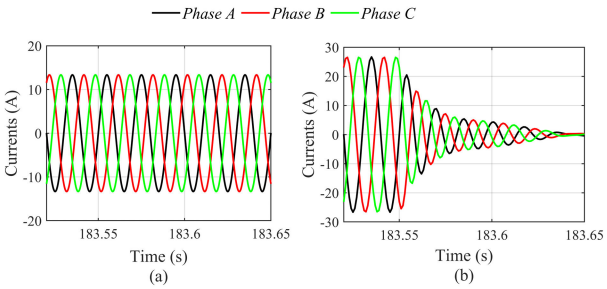

FIGURE 26. Load power quality during power shedding mode in S1: (a) currents injected to load 1, (b) currents injected to load 2.

V. EXPERIMENTAL RESULTS

The hardware-in-the-loop (HIL) setup is used to experimentally validate the proposed EMS and control strategies. The schematic layout of the HIL is described in Fig. 27, while the physical devices is shown in Fig. 28. The wave conditions and resulting WEC power outputs are emulated through MATLAB/Simulink simulations. Real-time execution of the control algorithms occurs on a dSPACE 1012 board processor integrated within a MicroAutobox System. A Chroma programmable AC power source is employed to replicate the EMF voltages associated with the simulated. The simulated EMF voltages are scaled down by a factor of 30 to be within the AC source's operational limits. The AC source outputs connect to inductors that mimic the inductance characteristics intrinsic to the PMLG stator windings. Consequently, currents passing through these inductors represent stator currents with a down scaling of 30. To compensate this down scaling, the F_{pto} computed by the MPPT algorithm is proportionally scaled down by a factor of 30 before being transmitted as i^*_{sq} to the current controllers. Conversely, the measured i_{sq} across the inductors is scaled up by an equivalent factor to realign F_{pto} with the virtual WEC model parameters. Two three-phase inverter modules interconnected via a DC-link capacitor constitute the back-to-back power conversion arrangement, while a Chroma bidirectional DC/DC power supply functions as a battery simulator. One inverter interfaces with the stator inductors, serving as the generator-side converter to maximize wave power extraction, while the second inverter functions as the load-side converter, facilitating DC/AC conversion for the load. A half-bridge inverter links the battery simulator to the DC bus capacitor, stabilizing the DC-link voltage and managing energy storage. The switching states are generated through sinusoidal pulse width modulation at a sampling frequency of 10 kHz. Real-time voltage and current measurements are acquired using USM-31V sensors. Table 4 details the parameters incorporated within this experiment.

The moderate and high-energy irregular waves, corresponding to S2 and S3 in Table 3, were used in the experimental validation to represent the stochastic characteristics of real sea conditions. These sea states were used to examine the transition between reactive and damping control modes, while S2 was additionally considered for the

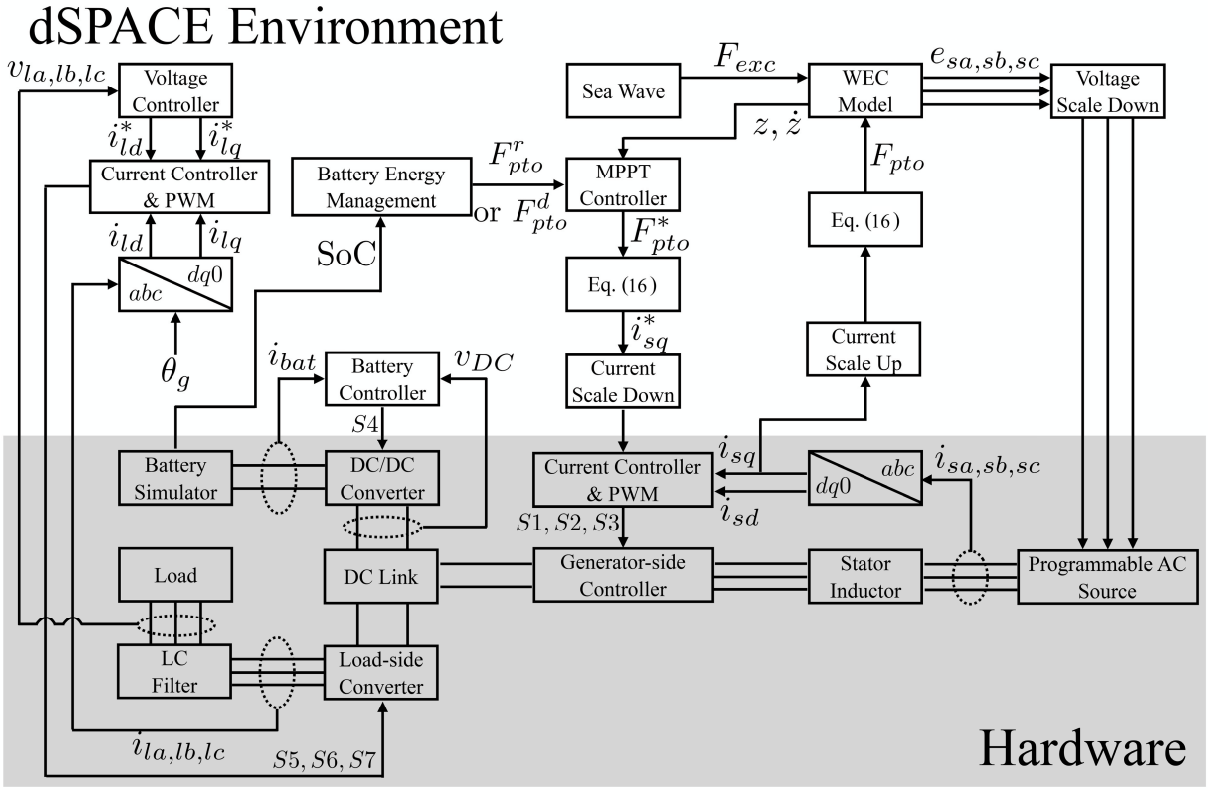

FIGURE 27. Depiction of the HIL scheme.

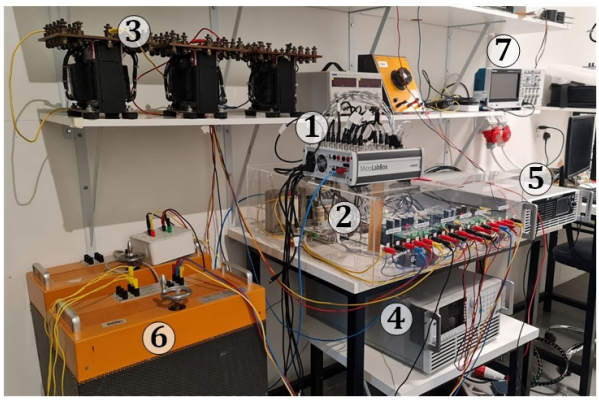

FIGURE 28. HIL experimental setup: (1) dSPACE MicroLabBox, (2) back to back converter configuration, (3) stator inductors, (4) Chroma programmable AC source, (5) battery simulator, (6) resistive load, (7) Oscilloscope.

TABLE 4. Hardware electrical parameters.

Parameter	Symbol (value)
Stator resistance	R_s (0.6 Ω)
Stator inductance	L_s (32 mH)
DC bus capacitor	C_{dc} (3.3 mF)
Nominal DC bus voltage	v_{dc} (150 V)
DC/DC Inductor resistance	R_b (30 mΩ)
DC/DC Inductor inductance	L_b (3.3 mH)
Battery voltage	v_{bat} (700 V)
Filter inductance	L_f (3.5 mH)
Filter capacitance	C_f (50 μF)
Load rms voltage	V_{rms} (35.36 V)
Fundamental frequency	f_0 (50 Hz)
Load power 1	$P_{l,1}$ (75 W)
Switching frequency	f_s (10 kHz)

load shedding assessment. The low-energy sea state (S1) was not included in the HIL experiments because, under the required down scaling factor of 30 imposed by the current and voltage limits of the power supply and converters, the generated power becomes very small. This leads to operation under light loading conditions that can hinder comprehensive performance assessment of the controllers and EMS operation. Figures 29 and 30 present the down scaled experimental results obtained under a S2. As predicted by (10) - (12), the emf voltage varies in magnitude and frequency with the translator position and wave excitation, reaching a maximum of approximately 46 V, while the corresponding three-phase stator currents attain peak values of about 2 A.

A. DAMPING AND REACTIVE CONTROL MODE TRANSITION

The WEC is subjected to S3 during the first 400 s, followed by S2 for the remaining 200 s. The battery simulator is initialized with a state of charge of 77%, and the load demand is maintained at 75 W throughout the experiment. Figure 31a

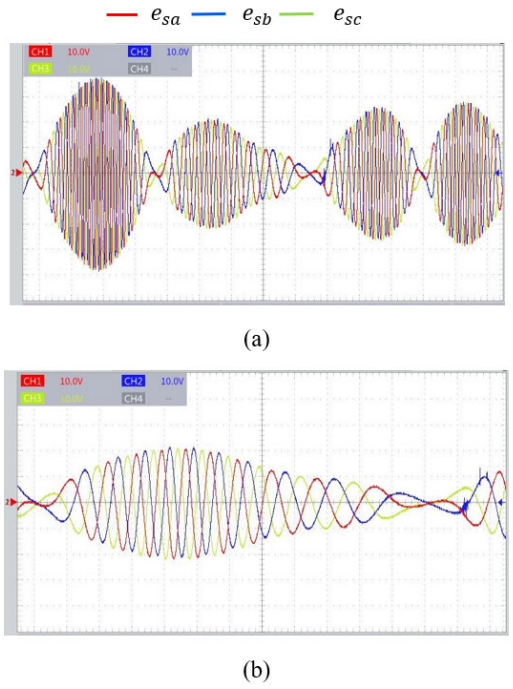

FIGURE 29. Experimental emf voltage measurements: (a) high time frame, (b) low time frame.

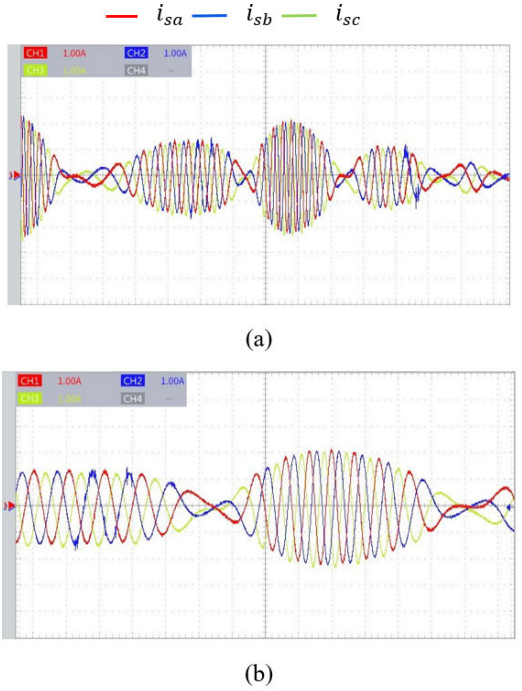

FIGURE 30. Experimental stator current measurements: (a) high time frame, (b) low time frame.

shows the resulting SoC trajectory, while Figure 31b displays the corresponding PTO coefficients, B_{pto} for damping and K_{pto} for stiffness. During the initial high-energy period, the EMS engages reactive control mode to maximize energy extraction. Both B_{pto} and K_{pto} are actively tuned, leading

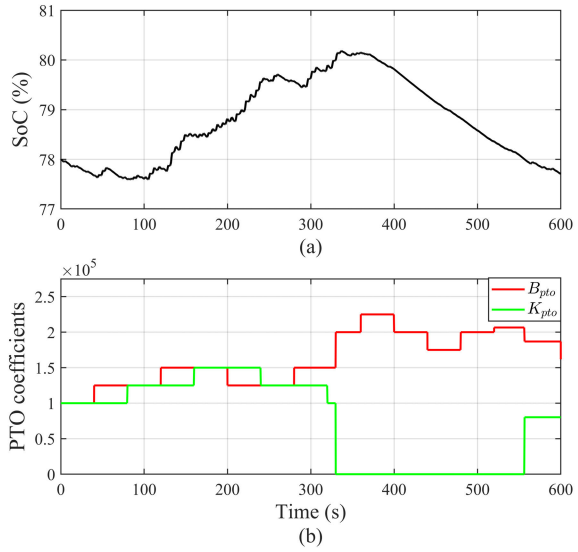

FIGURE 31. Experimental EMS validation during reactive and damping control transition: (a) state of charge, (b) PTO coefficients.

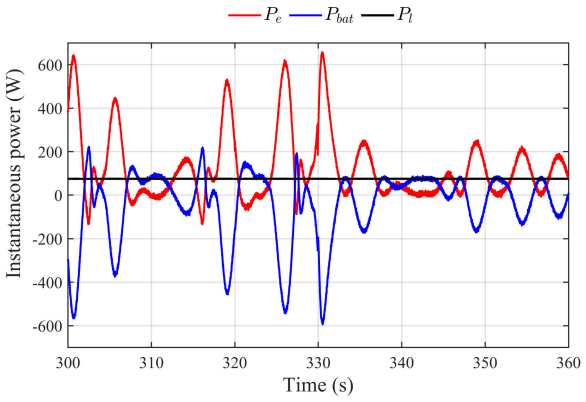

FIGURE 32. Instantaneous power behavior during reactive and damping control transition.

to a steady rise in SoC as P_e exceeds P_l. The SoC reaches $\text{SoC}_{max} \approx 80\%$ at around 329.8 s. To avoid overcharging the EMS switches to damping control mode and sets the stiffness coefficient K_{pto} to zero which leads to a rapid reduction in SoC. At 400 s the sea state changes to the moderate-energy condition S2 and the electrical power output P_e decreases. As expected, the MPPT responds by reducing the PTO damping coefficient to adapt to the reduced wave energy content. Since the EMS remains in damping mode the battery discharge becomes more pronounced. At approximately 556.1 s the SoC falls 2% below SoC_{max} which satisfies the predefined safety margin and triggers the reactivation of reactive control. The WEC then returns to maximum power operation but due to the lower energy content in S2 the P_e is not sufficient to meet the load demand and the SoC continues to decrease gradually.

Figure 32 illustrates the difference in instantaneous power behaviors between reactive and damping control. Before 329.8 s, P_e exhibits higher peaks and bidirectional

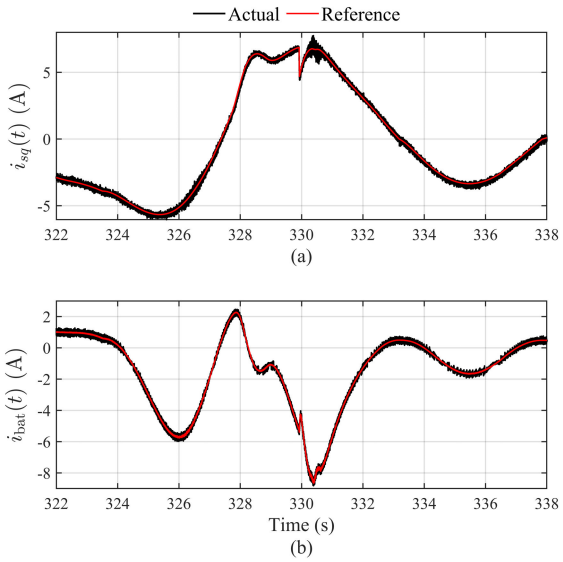

FIGURE 33. Experimental dynamic response of the inner current control loops during the transition from reactive to damping control: (a) PMLG quadrature current tracking, (b) battery current tracking.

behavior characteristic of reactive control. These strong power oscillations produce large negative P_{bat} values as the battery absorbs the excess energy, leading to an increase in SoC. After 329.8 s, when damping control is applied, P_e decreases and becomes unidirectional. The lower P_e requires greater battery contribution to meet P_l which causes gradual decrease in SoC.

Figure 33 presents the dynamic performance of the inner current control loops for the generator-side converter and the battery storage system during the transition from reactive to damping control. In Fig. 33a, the i_{sq} reference from the upper MPPT control loop drops abruptly from 6.8 A to 4.5 A due to the change in the computed control force, and then rises again to approximately 6.7 A. The inner current loop tracks these rapid variations with a brief overshoot to about 7.5 A during the rising phase, after which it quickly settles to the reference. This response reflects the higher bandwidth of the inner loop relative to the MPPT controller. Figure 33b shows that the battery current reference changes from −5.4 A to −4.1 A to support DC-link voltage regulation. The battery storage inner controller effectively follows this reference, ensuring stable operation during the control transition. Figure 34 shows the battery-side controller effectively regulated the DC-link voltage, maintaining v_{dc} close to 150 V, while the load-side controller ensured that the PCC phase voltages remain balanced and sinusoidal with a 50 V peak (35.36 V RMS). Figure 35 further verifies line currents exhibiting a 1 A peak amplitude at a 50 Hz fundamental frequency. Figure 36a presents the voltage harmonic spectrum, showing a total harmonic distortion (THD) of 2.1%, while Fig. 36b depicts the current harmonic spectrum with a THD of 2.9%. Both harmonic spectrums are dominated by the lower-order components namely the 3rd and 5th harmonics. According to IEEE Std. 519-2014 the THD limit for low-voltage systems is

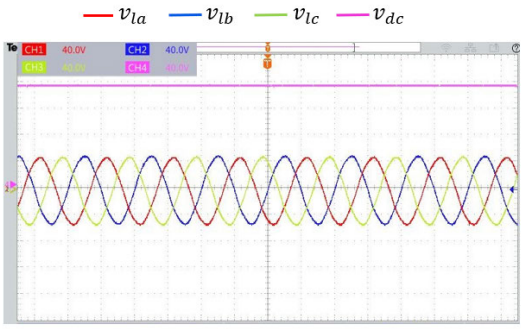

FIGURE 34. Experimental voltage measurements at the DC link and PCC.

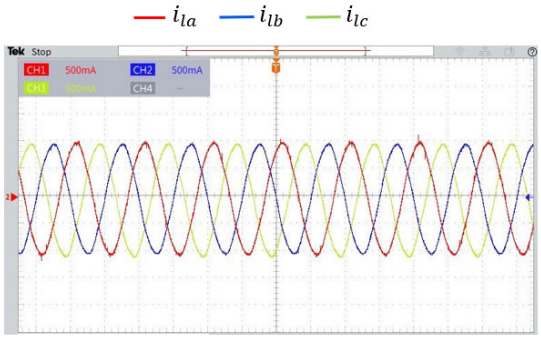

FIGURE 35. Experimental current measurements at the PCC.

5% for both voltage and current [67]. The measured values are well within this threshold which confirms that the LC filter satisfies power quality regulations.

B. POWER SHEDDING MODE

This subsection evaluates the effectiveness of the EMS in preventing deep battery discharge when the absorbed wave energy is insufficient to meet the load demand. As shown in Fig. 37b the running mean P_e remains between 20 and 30 W which is below the 75 W load demand. During this interval P_{bat} ranges approximately between 45 W and 60 W indicating sustained battery discharge to compensate for the power deficit. This condition leads to a steady decrease in SoC until it reaches 20% at about 279.7 s. At this point the EMS activates power shedding and disconnects the load. The battery discharge is then significantly reduced and the P_e is redirected to charge the battery which causes the SoC to increase. Once the SoC reaches the safe margin of 22% at approximately 481.5 s the load is reconnected. The SoC begins to decrease again since P_e remains insufficient to satisfy the load and the battery must supply the power shortfall.

Figure 38 shows the load shedding scenario carried out by the EMS. The power delivered to the load is maintained at approximately 75 W until the minimum SoC is reached, as seen in Fig. 38a. As a result, the EMS disconnects the load and the power drops directly to zero. Figure 38b presents $i_{ld}(t)$ which remains close to 1 A while the load is connected

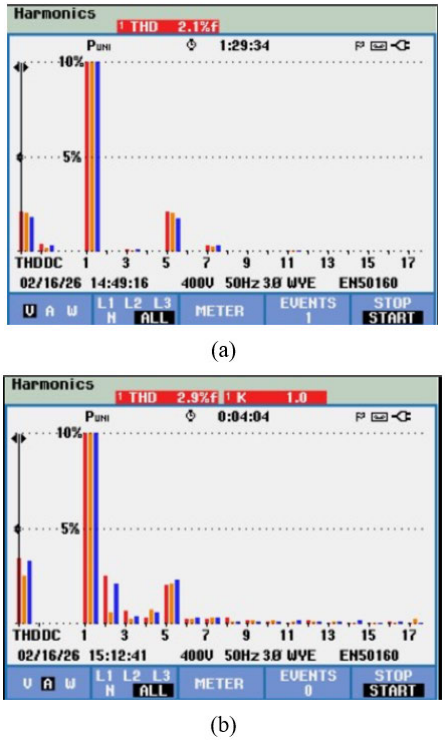

FIGURE 36. Total harmonic distortion at PCC: (a) voltage, (b) current.

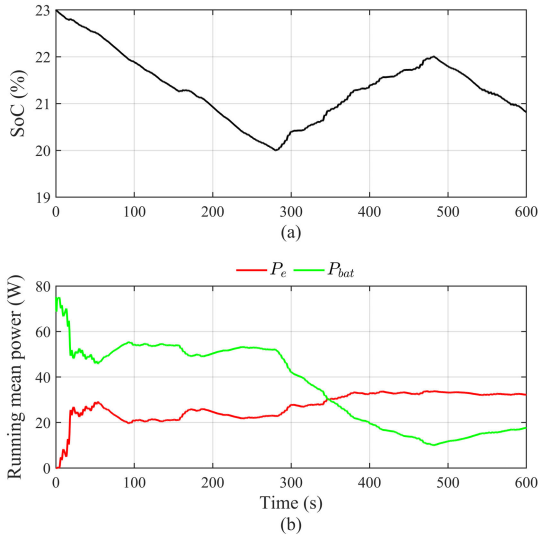

FIGURE 37. Experimental EMS performance under power shedding mode: (a) state of charge, (b) running mean power of P_e and P_{bat}.

and falls immediately to zero once the load is removed. This behavior follows the delivered power profile and confirms the direct correlation between them. The three-phase load currents at the moment of load disconnection are shown in Fig. 38c. Before 279.7 s the currents are balanced and sinusoidal. After the load is shed all phase currents collapse to nearly zero which indicates that no current is supplied to the load.

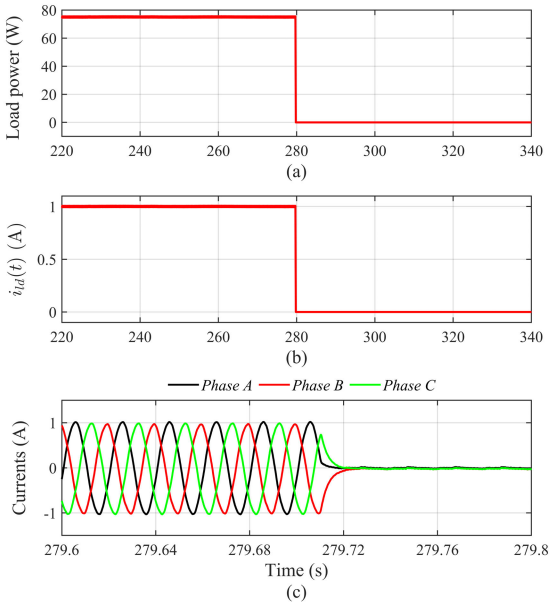

FIGURE 38. Experimental load-side subsystem response during power shedding mode: (a) Load power P_l, (b) direct-axis load current, (c) three-phase load currents.

VI. CONCLUSION

This paper presented a comprehensive control framework for the operation of a stand-alone WEC integrated with battery storage and load-side regulation. The proposed architecture leverages a tertiary EMS that dynamically switches between reactive control, damping control, and power shedding modes based on battery SoC and wave conditions. To maximize energy extraction, a variable step-size MPPT algorithm was employed to adaptively adjust the damping and stiffness coefficients, thereby enabling the implementation of damping and reactive control strategies. The battery-side controller effectively regulates the DC bus voltage by managing charge and discharge actions to maintain system stability under fluctuating conditions. Meanwhile, the load-side controller ensures high-quality three-phase power delivery with balanced voltage and current waveforms, preserving power quality during load transitions commanded by the EMS.

Simulation and experimental validations confirmed the controller's ability to maintain DC bus voltage stability, achieve balanced three-phase operation, and adapt to varying wave and load scenarios. Under high-energy waves, the EMS effectively maximized power generation and regulated SoC within operational bounds. In contrast, during low-energy scenarios, it successfully invoked load shedding to avoid deep battery discharge. The main contribution of this work lies in demonstrating an adaptive, battery-aware EMS that enables fully autonomous WEC operation in off-grid settings. Future research will investigate extending this control architecture to WEC arrays, enabling cooperative power management across multiple units as in wave farms. Additionally, the integration of hybrid energy storage systems—combining batteries with supercapacitors or other storage technologies will be explored to enhance transient stability.

REFERENCES

[1] G. Szustak, P. Dąbrowski, W. Gradoń, and Ł. Szewczyk, "The relationship between energy production and GDP: Evidence from selected European economies," *Energies*, vol. 15, no. 1, p. 50, Dec. 2021.

[2] *Tracking SDG7: The Energy Progress Report 2018.*, World Bank, Paris, France, 2018.

[3] E. I. Come Zebra, H. J. van der Windt, G. Nhumaio, and A. P. C. Faaij, "A review of hybrid renewable energy systems in mini-grids for off-grid electrification in developing countries," *Renew. Sustain. Energy Rev.*, vol. 144, Jul. 2021, Art. no. 111036.

[4] M. E. Khodayar, "Rural electrification and expansion planning of off-grid microgrids," *Electr. J.*, vol. 30, no. 4, pp. 68–74, May 2017.

[5] R. Pelc and R. Fujita, "Renewable energy from the ocean," *Mar. Policy*, vol. 26, no. 6, pp. 471–479, 2002.

[6] M. H. Jahangir, R. Alimohamadi, and M. Montazeri, "Performance comparison of pelamis, wavestar, langley, oscillating water column and Aqua buoy wave energy converters supplying islands energy demands," *Energy Rep.*, vol. 9, pp. 5111–5124, Dec. 2023.

[7] M. Vicente, A. Imperadore, F. X. Correia da Fonseca, M. Vieira, and J. Cândido, "Enhancing islanded power systems: Microgrid modeling and evaluating system benefits of ocean renewable energy integration," *Energies*, vol. 16, no. 22, p. 7517, Nov. 2023.

[8] D. Keiner, O. Salcedo-Puerto, E. Immonen, W. V. Sark, Y. Nizam, F. Shadiya, J. Duval, T. Delahaye, A. Gulagi, and C. Breyer, "Powering an island energy system by offshore floating technologies towards 100% renewables: A case for the Maldives," *Appl. Energy*, vol. 308, Feb. 2021, Art. no. 118360.

[9] S. Basnet, K. Deschinkel, L. L. Moyne, and M.-C. Péra, "A review on recent standalone and grid integrated hybrid renewable energy systems: System optimization and energy management strategies," *Renew. Energy Focus*, vol. 46, pp. 103–125, Sep. 2023.

[10] M. Jama, B. F. Mon, A. Wahyudie, and S. Mekhilef, "Maximum energy capturing approach for heaving wave energy converters using an estimator-based finite control set model predictive control," *IEEE Access*, vol. 9, pp. 67648–67659, 2021.

[11] R. G. Coe, G. Bacelli, and D. Forbush, "A practical approach to wave energy modeling and control," *Renew. Sustain. Energy Rev.*, vol. 142, May 2021, Art. no. 110791.

[12] M. Jama, A. Wahyudie, A. Assi, and H. Noura, "Controlling heaving wave energy converter using function-based model predictive control technique," in *Proc. 25th Chin. Control Decis. Conf. (CCDC)*, May 2013, pp. 2705–2710.

[13] A. de la Villa Jaén, D. E. M. Andrade, and A. García Santana, "Increasing the efficiency of the passive loading strategy for wave energy conversion," *J. Renew. Sustain. Energy*, vol. 5, no. 5, Sep. 2013, Art. no. 053132, doi: 10.1063/1.4824416.

[14] A. Wahyudie and M. A. Jama, "Perspectives on damping strategy for heaving wave energy converters," *IEEE Access*, vol. 5, pp. 22224–22233, 2017.

[15] M. Jama, A. Assi, A. Wahyudie, and H. Noura, "Self-tunable fuzzy logic controller for the optimization of heaving wave energy converters," in *Proc. Int. Conf. Renew. Energy Res. Appl. (ICRERA)*, Nov. 2012, pp. 1–6.

[16] E. Anderlini, D. I. M. Forehand, E. Bannon, Q. Xiao, and M. Abusara, "Reactive control of a two-body point absorber using reinforcement learning," *Ocean Eng.*, vol. 148, pp. 650–658, Jan. 2018.

[17] A. Wahyudie, O. Saeed, M. Jama, H. Noura, and K. Harib, "Maximising power conversion for heaving point absorbers using a reference-based control technique," *IET Renew. Power Gener.*, vol. 11, no. 3, pp. 271–280, Feb. 2017.

[18] E. Amon, A. A. Schacher, and T. Brekken, "A novel maximum power point tracking algorithm for ocean wave energy devices," in *Proc. IEEE Energy Convers. Congr. Expo. (ECCE)*, Nov. 2009, pp. 2635–2641.

[19] X. Yue, D. Geng, Q. Chen, Y. Zheng, G. Gao, and L. Xu, "2-D lookup table based MPPT: Another choice of improving the generating capacity of a wave power system," *Renew. Energy*, vol. 179, pp. 625–640, Dec. 2021.

[20] E. A. Amon, T. K. A. Brekken, and A. A. Schacher, "Maximum power point tracking for ocean wave energy conversion," *IEEE Trans. Ind. Appl.*, vol. 48, no. 3, pp. 1079–1086, May 2012.

[21] M. Jama and A. Wahyudie, "Online damping strategy for controlling heaving wave energy converters using three-phase bridge boost rectifier," *IEEE Access*, vol. 5, pp. 7682–7691, 2017.

[22] B. F. Mon, A. Wahyudie, M. A. Jama, S. Akbar, S. Mekhilef, H. Shareef, K. Harib, and R. Errouissi, "Assessment of damping control using maximum power point tracking methods for heaving wave energy converters," *IEEE Access*, vol. 9, pp. 168907–168921, 2021.

[23] X. Xiao, X. Huang, and Q. Kang, "A hill-climbing-method-based maximum-power-point-tracking strategy for direct-drive wave energy converters," *IEEE Trans. Ind. Electron.*, vol. 63, no. 1, pp. 257–267, Jan. 2016.

[24] A. Y. Elamin, A. Wahyudie, T. B. Hashfi, H. Shareef, R. Errouissi, M. S. Laghari, M. B. Mubin, and S. Mekhilef, "MPPT reactive control algorithm for heaving wave energy converters with power setpoint capabilities," *IEEE Access*, vol. 12, pp. 176779–176798, 2024.

[25] S. Dong and Z. Wu, "Prescribed performance adaptive MPPT control of direct-drive wave energy generation system," *Ocean Eng.*, vol. 298, Apr. 2024, Art. no. 117066.

[26] W. Zhong, M. Zhang, J. Zhang, J. Liu, and H. Yu, "Constrained MPPT strategy for sustainable wave energy converters with magnetic lead screw," *Sustainability*, vol. 16, no. 11, p. 4847, Jun. 2024.

[27] G. Yao, Z. Luo, Z. Lu, M. Wang, J. Shang, and J. M. Guerrerob, "Unlocking the potential of wave energy conversion: A comprehensive evaluation of advanced maximum power point tracking techniques and hybrid strategies for sustainable energy harvesting," *Renew. Sustain. Energy Rev.*, vol. 185, Oct. 2023, Art. no. 113599.

[28] O. Saeed, A. Wahyudie, T. B. Susilo, and H. Shareef, "Simple resonance circuit to improve electrical power conversion in a two-sided planar permanent magnet linear generator for wave energy converters," *IEEE Access*, vol. 5, pp. 18654–18664, 2017.

[29] S. R. Sinsel, R. L. Riemke, and V. H. Hoffmann, "Challenges and solution technologies for the integration of variable renewable energy sources—A review," *Renew. Energy*, vol. 145, pp. 2271–2285, Jan. 2020.

[30] M. Beaudin, H. Zareipour, A. Schellenberglabe, and W. Rosehart, "Energy storage for mitigating the variability of renewable electricity sources: An updated review," *Energy for Sustain. Develop.*, vol. 14, no. 4, pp. 302–314, Dec. 2010.

[31] Y. Li, X. Wang, X. Fang, Y. Liu, P. Zhao, and R. Cui, "Modeling and control strategy analysis of a hydraulic energy-storage wave energy conversion system," *Renew. Energy*, vol. 182, pp. 969–981, Jan. 2022.

[32] A. Y. Elamin and A. Wahyudie, "Optimal control of a supercapacitor energy storage system for smoothing wave output power," in *Proc. Int. Conf. Electr. Comput. Technol. Appl. (ICECTA)*, Nov. 2022, pp. 186–189.

[33] N. H. Samrat, N. B. Ahmad, I. A. Choudhury, and Z. B. Taha, "Modeling, control, and simulation of battery storage photovoltaic-wave energy hybrid renewable power generation systems for island electrification in Malaysia," *Sci. World J.*, vol. 2014, pp. 1–21, Apr. 2014.

[34] S. Rasool, K. M. Muttaqi, and D. Sutanto, "A multi-filter based dynamic power sharing control for a hybrid energy storage system integrated to a wave energy converter for output power smoothing," *IEEE Trans. Sustain. Energy*, vol. 13, no. 3, pp. 1693–1706, Jul. 2022.

[35] M. F. Zia, M. Nasir, E. Elbouchikhi, M. Benbouzid, J. C. Vasquez, and J. M. Guerrero, "Energy management system for a hybrid PV-wind-tidal-battery-based islanded DC microgrid: Modeling and experimental validation," *Renew. Sustain. Energy Rev.*, vol. 159, May 2022, Art. no. 112093.

[36] A. Parwal, M. Fregelius, I. Temiz, M. Göteman, J. G. D. Oliveira, C. Boström, and M. Leijon, "Energy management for a grid-connected wave energy park through a hybrid energy storage system," *Appl. Energy*, vol. 231, pp. 399–411, Dec. 2018.

[37] J. Schmalstieg, S. Käbitz, M. Ecker, and D. U. Sauer, "A holistic aging model for Li(NiMnCo)O_2 based 18650 lithium-ion batteries," *J. Power Sources*, vol. 257, pp. 325–334, Jul. 2014.

[38] C. R. Birkl, M. R. Roberts, E. McTurk, P. G. Bruce, and D. A. Howey, "Degradation diagnostics for lithium-ion batteries: Capacity fade and internal resistance increase," *J. Power Sources*, vol. 341, pp. 373–386, Feb. 2017.

[39] M. Ecker, N. Nieto, S. Käbitz, J. Schmalstieg, H. Blanke, A. Warnecke, and D. U. Sauer, "Calendar and cycle life study of Li(NiMnCo)O_2-based 18650 lithium-ion batteries," *J. Power Sources*, vol. 248, pp. 839–851, Feb. 2014.

[40] J. Wang, P. Liu, J. Hicks-Garner, E. Sherman, S. Soukiazian, M. Verbrugge, H. Tataria, J. Musser, and P. Finamore, "Cycle-life model for graphite-$LiFePO_4$ cells," *J. Power Sources*, vol. 196, no. 8, pp. 3942–3948, Apr. 2011.

[41] K. Divya and J. Østergaard, "Battery energy storage technology for power systems—An overview," *Electric Power Syst. Res.*, vol. 79, no. 4, pp. 511–520, 2008.
[42] H. Rahimi-Eichi, U. Ojha, F. Baronti, and M.-Y. Chow, "Battery management system: An overview of its application in the smart grid and electric vehicles," *IEEE Ind. Electron. Mag.*, vol. 7, no. 2, pp. 4–16, Jun. 2013.
[43] K. B. Samal, S. Pati, and R. Sharma, "Power management using an improved EMS algorithm in a stand-alone hybrid PV-PEMFC microgrid with reduced converter count," *Green Energy Intell. Transp.*, vol. 5, no. 2, 2025, Art. no. 100302.
[44] R. Gugulothu, B. Nagu, and D. Pullaguram, "Energy management strategy for standalone DC microgrid system with photovoltaic/fuel cell/battery storage," *J. Energy Storage*, vol. 57, Jan. 2023, Art. no. 106274.
[45] L. Martínez-Caballero, A. Aslam, R. Kot, A. Milczarek, and M. Malinowski, "A control strategy for a standalone PV-battery system operating at SoC boundaries with DC-link ripple management," *IEEE Access*, vol. 13, pp. 183706–183721, 2025.
[46] P. Kamat, S. Hazra, and S. Bhattacharya, "Stand-alone low-cost wave energy generation with energy storage integration," in *Proc. IEEE Appl. Power Electron. Conf. Expo. (APEC)*, Mar. 2017, pp. 1550–1557.
[47] D. Pelosi, F. Gallorini, G. Alessandri, and L. Barelli, "A hybrid energy storage system integrated with a wave energy converter: Data-driven stochastic power management for output power smoothing," *Energies*, vol. 17, no. 5, p. 1167, 2024.
[48] M. Jama, A. Wahyudie, H. Shareef, and Md E. Haque, "Wave-togrid hierarchical coordinated control with energy storage and management for point absorber wave energy converters," *Energy Convers. Manage.: X*, vol. 27, Jul. 2025, Art. no. 101125, doi: 10.1016/j.ecmx.2025.101125.
[49] B. Yang, J. Duan, Y. Chen, S. Wu, M. Li, P. Cao, and L. Jiang, "A critical survey of power take-off systems based wave energy converters: Summaries, advances, and perspectives," *Ocean Eng.*, vol. 298, Nov. 2024, Art. no. 117149.
[50] X. Li, C.-A. Chen, Q. Li, L. Xu, C. Liang, K. D. T. Ngo, R. G. Parker, and L. Zuo, "A compact mechanical power take-off for wave energy converters: Design, analysis, and test verification," *Appl. Energy*, vol. 278, 2020, Art. no. 115459.
[51] K. Rhinefrank, A. Schacher, J. Prudell, T. K. A. Brekken, C. Stillinger, and J. Z. Yen, "Comparison of direct-drive power take-off systems for ocean wave energy applications," *IEEE J. Oceanic Eng.*, vol. 37, no. 1, pp. 35–44, Jan. 2012.
[52] S. Rezaei, A. Rahimi, J. Parvizian, S. Mansoorzadeh, and A. Düster, "A rectified unidirectional rotary PTO for two-body wave energy converters," *Ocean Eng.*, vol. 279, pp. 1–10, Jul. 2023.
[53] O. Farrok, Md. R. Islam, Md. R. Islam Sheikh, Y. Guo, J. Zhu, and W. Xu, "A novel superconducting magnet excited linear generator for wave energy conversion system," *IEEE Trans. Appl. Supercond.*, vol. 26, no. 7, pp. 1–5, Oct. 2016.
[54] M. C. Sousounis and J. Shek, "Wave-to-wire power maximization control for all-electric wave energy converters with non-ideal power take-off," *Energies*, vol. 12, no. 15, p. 2948, Jul. 2019.
[55] I. Boldea and S. A. Nasar, *Linear Electric Actuators and Generators*. Cambridge, U.K.: Cambridge Univ. Press, 1997.
[56] P. S. Kumar, R. P. S. Chandrasena, V. Ramu, G. N. Srinivas, and K. V. S. M. Babu, "Energy management system for small scale hybrid wind solar battery based microgrid," *IEEE Access*, vol. 8, pp. 8336–8345, 2020.
[57] R. Guo and W. Shen, "A review of equivalent circuit model based online state of power estimation for lithium-ion batteries in electric vehicles," *Vehicles*, vol. 4, no. 1, pp. 1–29, Dec. 2021.
[58] R. Vieira, P. Kollmeyer, L. Pitault, and A. Emadi, "Comprehensive comparison of machine learning and Kalman filter battery state of charge estimators," *IEEE Access*, vol. 13, pp. 36321–36338, 2025.
[59] T.-U. Rehman and C. W. Park, "Progress in insulated gate bipolar transistor thermal management: From fundamentals to advanced strategies," *Renew. Sustain. Energy Rev.*, vol. 210, Mar. 2025, Art. no. 115219.
[60] S. Salter, J. Taylor, and N. Caldwell, "Power conversion mechanisms for wave energy," *Proc. Inst. Mech. Engineers*, vol. 216, no. 1, pp. 1–27, 2002.
[61] P. B. Garcia-Rosa, J. V. Ringwood, O. B. Fosso, and M. Molinas, "The impact of time–frequency estimation methods on the performance of wave energy converters under passive and reactive control," *IEEE Trans. Sustain. Energy*, vol. 10, no. 4, pp. 1784–1792, Oct. 2019.
[62] H. Wang and F. Blaabjerg, "Reliability of capacitors for DC-link applications in power electronic converters—An overview," *IEEE Trans. Ind. Appl.*, vol. 50, no. 5, pp. 3569–3578, Sep. 2014.
[63] R.-J. Wai, C.-Y. Lin, Y.-C. Huang, and Y.-R. Chang, "Design of high-performance stand-alone and grid-connected inverter for distributed generation applications," *IEEE Trans. Ind. Electron.*, vol. 60, no. 4, pp. 1542–1555, Apr. 2013.
[64] T. B. Hashfi, A. Wahyuddie, A. Y. Elamin, B. F. Mon, and S. Akbar, "Energy management for single machine permanent magnet linear generator (PMLG) for stand-alone application," in *Proc. Int. Conf. Control, Commun. Comput. (ICCC)*, May 2023, pp. 1–6.
[65] O. M. Mohemed, "Maximising capture power battery manage. For heaving wave energy converters," Doctorate dissertation, Dept. Elect. Commun. Eng., United Arab Emirates Univ., AlAin, UAE, Dec. 2023.
[66] A. Pecher and J. P. Kofoed, *Handbook Ocean Wave Energy*. Cham, Switzerland: Springer, 2017.
[67] R. Langella, A. Testa, and E. Alii, *IEEE Recommended Practice and Requirements for Harmonic Control in Electric Power Systems*, Standard IEEE SM 519-1992, 2014.

ABDIN YOUSIF ELAMIN received the B.Eng. degree (Hons.) in mechatronics engineering from International Islamic University Malaysia, in 2014, the M.Eng. degree in mechatronics and automatic control from the University of Technology Malaysia, in 2017, and the Ph.D. degree in electrical engineering from United Arab Emirates University, in 2023. In 2018, he was a Lecturer with the Control Department, University of Medical Science and Technology, Sudan. Currently, he is a Research Associate with United Arab Emirates University. His research interests include model predictive control, artificial intelligence, and control applications in renewable energy and electromechanical systems.

TUANKU BADZLIN HASHFI (Graduate Student Member, IEEE) received the B.Eng. degree (Hons.) in electrical and electronics engineering from the National University of Malaysia, Selangor, Malaysia, in 2015, and the M.Eng.Sc. degree from the University of Malaya, Malaysia, in 2021. He is currently pursuing the Ph.D. degree with TU Delft, The Netherlands. Then, he was with United Emirates Arab University (UAEU), as a Research Assistant until June 2024. His research interests include dc/dc converters, ac/dc converters, multilevel converters, modular multilevel converters (MMC), the control strategies, renewable energy conversion, and high voltage direct current (HVDC).

OMSALAMA M. MOHAMED received the B.Sc., M.Sc., and Ph.D. degrees in electrical engineering from United Arab Emirates University (UAEU), Al Ain, United Arab Emirates, in 1995, 2015, and 2023, respectively. She was a Teaching Assistant with UAEU, from 1997 to 2000, and a Research Assistant, from 2014 to 2023. She was a part-time Instructor with the University of Dubai. Her research interests include renewable energy systems, wave energy converters, battery energy management strategies, permanent magnet linear generators, and control techniques for energy applications. She has experience in modeling, simulation, and hardware-in-the-loop (HIL) validation.

ADDY WAHYUDIE received the B.Eng. degree in electrical engineering from the Universitas Gadjah Mada, Indonesia, in 2002, the M.Eng. degree in electrical engineering from Chulalongkorn University, Thailand, in 2005, and the Dr.Eng. degree in electrical engineering from Kyushu University, Japan, in 2010. From 2005 to 2011, he was a Lecturer with the Department of Electrical Engineering, Universitas Gadjah Mada. In 2011, he joined United Arab Emirates University (UAEU), as an Assistant Professor, where he is currently an Associate Professor with the Department of Electrical and Communication Engineering. His research interests include control system applications in electromechanical systems and renewable energy technologies.

ADHA IMAM CAHYADI received the bachelor's degree in electrical engineering from the Universitas Gadjah Mada, Indonesia, in 2002, the master's degree in control engineering from KMITL, Thailand, in 2005, and the Ph.D. degree in precision mechanics engineering from Tokai University, Japan, in 2008. From 2009 to 2011, he was a Postdoctoral Fellow with the Centre for Robotics and Artificial Intelligence (CAIRO), Universiti Teknologi Malaysia, Kuala Lumpur. In 2011, he joined the Department of Electrical Engineering, Universitas Gadjah Mada, as a Lecturer. He is currently an Associate Professor and the Chairperson of the bachelor's program.

MOHAMED ABDI JAMA (Member, IEEE) received the B.S. and Ph.D. degrees in electrical engineering from UAE University, Al Ain, United Arab Emirates, in 2009 and 2015, respectively. From 2015 to 2018, he was a Postdoctoral Fellow with the Department of Electrical Engineering, UAE University, where he was an Adjunct Faculty Member. From 2018 to 2021, he was a Research Fellow with the National Water and Energy Center (NWEC), UAE University. He is currently an Assistant Professor with the Department of Electrical, Computer, and Biomedical Engineering (ECBE), Abu Dhabi University, United Arab Emirates. His research interests include power systems, energy conversion, and control systems, focusing on the modeling, control, and analysis of renewable energy systems, including solar, wind, and marine energy, and microgrids and grid-scale energy storage systems. He is a fellow of the Higher Education Academy (FHEA) and a member of the IEEE Power and Energy Society (PES). He is also a Certified Renewable Energy Professional (REP) from the Association of Energy Engineers (AEE).

MOHAMMAD SHAKEEL LAGHARI received the B.E. degree in electronic engineering from the Mehran University of Engineering and Technology, Jamshoro, Pakistan, in 1980, the M.S. degree in electrical engineering from Drexel University, Philadelphia, PA, USA, in 1983, and the Ph.D. degree in computer engineering from the University of Wales, Swansea, Wales, U.K., in 1993. He was an Assistant Professor at Kuwait and King Saud universities. He is currently an Associate Professor with the Department of Electrical and Communication Engineering, United Arab Emirates University, Al Ain, United Arab Emirates. His research interests include applied artificial intelligence, image processing, and software systems. He has published more than 90 papers in these areas. He is a member of IACSIT (Singapore), P.E.C. (Pakistan), UACEE (USA), and IRED (USA).

RUHUL AMIN KHALIL received the Ph.D. degree in electrical engineering from the Department of Electrical Engineering, Faculty of Electrical and Computer Engineering, University of Engineering and Technology, Peshawar, Pakistan, in 2021. He was a Postdoctoral Research Fellow with the Department of Electrical and Communication Engineering, UAE University, Al Ain, United Arab Emirates, from 2023 to 2024. He is currently a Lecturer with the Engineering Requirement Unit (ERU), College of Engineering, UAE University. His research interests include the Internet of Things, machine learning, large language models, dimensionality reduction, localization, network traffic estimation, software-defined networks, and underwater wireless communication.

SAAD MEKHILEF (Fellow, IEEE) received the B.Eng. degree in electrical engineering from the University of Sétif, Sétif, Algeria, in 1995, and the master's degree in engineering science and the Ph.D. degree in electrical engineering from the University of Malaya, Kuala Lumpur, Malaysia, in 1998 and 2003, respectively. He is currently a Professor and the Director of the Power Electronics and Renewable Energy Research Laboratory, Department of Electrical Engineering, University of Malaya. He is also the Dean of the Faculty of Engineering, University of Malaya. He is also a Distinguished Adjunct Professor with the School of Software and Electrical Engineering, Faculty of Science, Engineering and Technology, Swinburne University of Technology, VIC, Australia. He has authored more than 450 publications in international journals and conference proceedings. His current research interests include power converter topologies, control of power converters, renewable energy, and energy efficiency.

AHMED ABDRABOU received the B.Sc. degree in electrical engineering from Ain Shams University, Egypt, in 1995, and the M.Eng. degree in electrical engineering from the Universiti Teknologi Malaysia (UTM), Johor Bahru, Malaysia, in 2014. He is currently pursuing the Ph.D. degree in electrical engineering with United Arab Emirates University (UAEU), Al Ain, United Arab Emirates. He is also a Laboratory Engineer with the Department of Electrical and Communication Engineering, UAEU. His professional background includes roles in electrical planning, maintenance, and commissioning. His research interests include smart grids, renewable energy integration, monitoring and detection of pre-fault and partial discharges, and grid-tied multilevel inverter systems.